

₁ Physics-Infused Reduced-Order Modeling for Analysis of
₂ Ablating Hypersonic Thermal Protection Systems

₃

₄ November 29, 2025

₅

Abstract

₆ This work presents a *physics-infused reduced-order modeling* (PIROM) framework
₇ towards design, analysis, and optimization of non-decomposing ablating hypersonic
₈ thermal protection systems (TPS), and is demonstrated via the modeling of transient
₉ thermo-ablative responses of multi-layered hypersonic TPS. The PIROM architecture
₁₀ integrates a *reduced-physics model* (RPM) as the building block, which is based on
₁₁ the *lumped capacitance model* (LCM) coupled to a *surface recession model* (SRM).
₁₂ The RPM provides a low-fidelity estimate of the thermo-ablative response of the TPS,
₁₃ based on average temperatures and one-dimensional surface displacements. This RPM
₁₄ is extended with data-driven hidden dynamics that are formulated via a systematic
₁₅ coarse-graining approach rooted in the *Mori-Zwanzig* (MZ) formalism, and that are
₁₆ learned from high-fidelity simulation data. Therefore, while the LCM and SRM capture
₁₇ the dominant physics of the ablating TPS response, the correction terms compensate for
₁₈ residual dynamics arising from higher-order non-linear interactions and temperature-
₁₉ advection effects due to surface recession. The trained PIROM consistently achieves
₂₀ errors of $\approx 0.5\%$ for a wide range of extrapolative settings of design parameters involv-
₂₁ ing time-and-space varying boundary conditions and SRM models, and improves by an
₂₂ order of magnitude by the LCM alone. Moreover, the PIROM delivers RPM-level com-
₂₃ putational costs, enabling evaluations that are two orders of magnitude faster than
₂₄ the high-fidelity full-order model (FOM). These results demonstrate that PIROM ef-
₂₅ fectively reconciles the trade-offs between accuracy, generalizability, and efficiency, pro-
₂₆ viding a promising framework for optimizing multi-physical dynamical systems, such
₂₇ as TPS, under diverse operating conditions.

₂₈

1 Introduction

₂₉ At hypersonic speeds, aerospace vehicles experience extreme aero-thermo-dynamic environ-
₃₀ ments that require specialized thermal protection systems (TPS) to shield internal sub-
₃₁ structures, electronics, and possibly crew members from the intense aerodynamic heating.
₃₂ The TPS is composed of ablating materials to withstand the high-energy physics – a high-
₃₃ temperature-capable and fibrous material injected with a resin that fills the pore network
₃₄ and strengthens the composite [1]. The TPS design promotes the exchange of mass through
₃₅ thermal and chemical reactions (i.e., ablation), effectively mitigating heat transfer to the

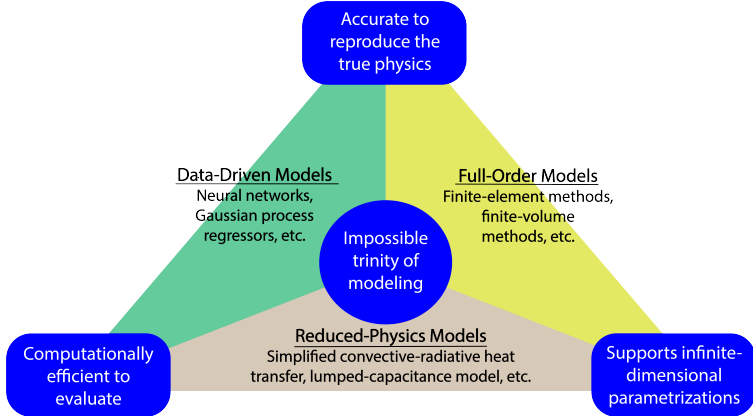


Figure 1: The impossible trinity of modeling: accuracy, generalizability, and efficiency.

36 sub-structures. As a result, accurate prediction for the ablating TPS response under ex-
37 treme hypersonic heating becomes critical to ensuring survivability, performance, and safety
38 of hypersonic vehicles.

39 Even with today’s advancements in computational resources and numerical methods,
40 high-fidelity simulations of ablating TPS remains a formidable challenge, both theoreti-
41 cally and computationally. On the theoretical side, the thermo-chemical reactions, coupled
42 with the irregular pore network structure and ablating boundaries, translate into complex
43 non-linear equations governing multi-physical interactions across several spatio-temporal
44 scales [1, 8]. On the computational side, numerical approaches based on finite-element
45 (FEM) or finite-volume (FVM) methods yield systems of differential equations modeling the
46 transient thermo-ablative response of the TPS [5]. The FEM discretizations lead to high-
47 dimensional systems of equations, resulting in prohibitive computational costs for many-
48 query applications such as design, optimization, uncertainty quantification, and real-time
49 applications, where possibly thousands of model evaluations are required.

50 Reduced-order models (ROMs) have emerged as a promising approach to alleviate the
51 computational costs of high-fidelity simulations [6, 11]. Ideally, a ROM should be: (1)
52 accurate to reproduce high-fidelity solutions, (2) support continuous or infinite-dimensional
53 design parameters such as geometrical shapes and material distributions, (3) be computa-
54 tionally efficient to evaluate to allow for fast turnaround times in design optimization. However,
55 the above three capabilities usually form an *impossible trinity of modeling*, as illustrated in
56 Fig. 1; building a ROM that achieves any two capabilities sacrifices the third.

57 The impossible trinity poses a significant challenge in the development of ROMs for
58 the multi-disciplinary transient analysis and optimization of ablating TPS. Specifically, full-
59 order models (FOMs), e.g., FEMs or FVMs, offer high accuracy and robust generalization
60 over design spaces, but are computationally expensive to evaluate. Reduced-physics models
61 (RPMs) – such as simplified convective-radiative heat transfer or engineering correlations –
62 are low-dimensional models that achieve efficiency and broad applicability by ignoring higher-
63 order non-linear effects. However, RPMs sacrifice accuracy for complex thermo-ablative
64 responses due to the simplifications and assumptions inherent in their formulation, and it
65 is generally not clear how to systematically leverage existing high-fidelity data to improve
66 RPMs [19].

67 Lastly, data-driven ROMs, such as Gaussian Process Regression (GPR) [16], Neural Net-
68 works (NNs), and neural ordinary differential equations (NODEs) [3], can provide accurate
69 and computationally-efficient approximations of high-fidelity models for complex thermo-
70 ablative responses. However, these data-centric approaches often demand extensive high-
71 fidelity data for training, do not necessarily satisfy fundamental physical constraints or con-
72 servation laws, and thus do not generalize well to the design spaces outside the training [17].
73 For example, our previous work demonstrated that NODEs trained on high-fidelity data of
74 non-ablating TPS failed to generalize when subjected to boundary conditions and material
75 models outside the training set [18].

76 This work presents the extension of the *physics-infused reduced-order modeling* (PIROM)
77 framework to include effects of ablation for TPS applications, previously ignored in Ref. [18].
78 Specifically, the PIROM is demonstrated for the transient thermo-ablative response of multi-
79 layered hypersonic TPS. The PIROM is a non-intrusive framework that combines the strengths
80 of physics-based models with machine learning to formulate and train ROMs for parametrized
81 non-linear dynamical systems. The backbone of the PIROM is the physics-based component,
82 i.e., the RPM, which in this work is composed of: (1) a *lumped capacitance model* (LCM)
83 to model the average heat transfer within the TPS layers, and (2) a *surface recession model*
84 (SRM) to model one-dimensional surface ablation.

85 Leveraging the *Mori-Zwanzig* (MZ) formalism [15, 14, 13], the RPM is rigorously ex-
86 tended with data-driven hidden dynamics to account for the missing physics in the LCM,
87 which are learned from high-fidelity data. The hidden dynamics enable higher predictive
88 accuracy of the PIROM when subjected to complex boundary conditions and SRM model
89 variations. For the TPS problem, the MZ approach produces a sufficiently simple model
90 form while maintaining the physical consistency of the PIROM, as well as the dependence
91 on design parameters. Thus, the PIROM aims to solve the ITM by leveraging the gen-
92 eralizability and computational efficiency of RPMs, while incorporating the accuracy and
93 adaptability of data-driven extensions. More importantly, the PIROM formulation provides
94 a general methodology for developing PIROMs for other multi-physics problems.

95 The specific objectives of this work are summarized as follows:

- 96 1. Extend the previous PIROM formulation in Ref. [18] to model transient thermo-
97 ablative response of multi-layered hypersonic TPS through a systematic coarse-graining
98 procedure based on the Mori-Zwanzig formalism.
- 99 2. Benchmark the accuracy, generalizability, and computational accelerations of the PIROM
100 against the RPM and the high-fidelity FEM solutions of ablating TPS, thus quanti-
101 fying the PIROM’s capabilities to solve the ITM in complex multi-physical non-linear
102 dynamical systems.

103 2 Modeling of Thermal Protection Systems

104 This section presents the problem of modeling the transient thermo-ablative response of a
105 non-decomposing TPS, subjected to extreme hypersonic heating. Two different but math-
106 ematically connected solution strategies are provided: (1) a high-fidelity full-order model

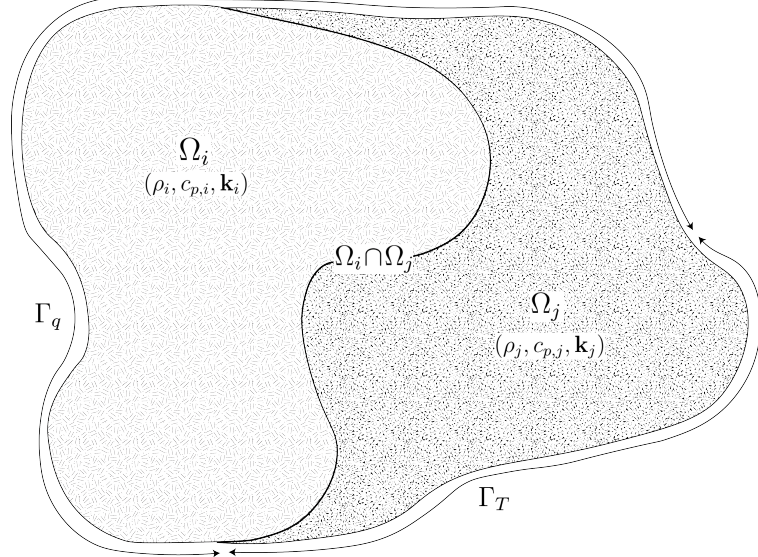


Figure 2: General domain Ω with prescribed Neumann and Dirichlet boundary conditions on Γ_q and Γ_T . Mesh displacement $w(x, t)$ occurs on the Γ_q boundary.

107 (FOM) based on a finite element method (FEM), and (2) a RPM based on a *lumped capacitance model* (LCM) coupled with a one-dimensional *surface recession model* (SRM). The
108 FOM is computationally expensive but provides the highest fidelity, while the RPM is com-
109 putationally efficient but has low predictive fidelity. However, both models are physically
110 consistent to high-dimensional design variables. The following discussion presents the TPS
111 modeling problem and the FOM and RPM solution strategies.
112

113 2.1 Governing Equations

114 The multi-physics of a non-decomposing ablating TPS under a hypersonic boundary layer
115 involves the *energy equation* for heat conduction inside the TPS, and the *pseudo-elasticity*
116 *equation* for mesh motion due to surface recession. The coupling between these two equations
117 occurs at the heated boundary, where the surface temperature drives the surface recession
118 velocity, which appears as an advection term in the energy equation. The governing PDEs
119 are described as follows.

120 2.1.1 Energy Equation

121 Consider a generic domain $\Omega \subset \mathbb{R}^d$, $d = 2$ or 3 , illustrated in Fig. 2. Let $\partial\Omega = \Gamma_q \cup \Gamma_T$
122 and $\Gamma_q \cap \Gamma_T = \emptyset$, where a Neumann $q_b(x, t)$ boundary condition is prescribed on the heated
123 boundary Γ_q , and represents the surface exposed to the hypersonic boundary layer. The
124 Dirichlet $T_b(x, t)$ boundary condition is prescribed on the boundary Γ_T . The TPS is divided
125 into N non-overlapping components $\{\Omega_i\}_{i=1}^N$, as illustrated in Fig. 2 for $N = 2$. The i -th
126 component Ω_i is associated with material properties $(\rho_i, c_{p,i}, \mathbf{k}_i)$, which are continuous within
127 one component, and can be discontinuous across two neighboring components.

128 Over the time domain $\mathcal{T} = [t_0, t_f]$, the energy equation describes the transient heat

¹²⁹ conduction inside the TPS,

$$\rho c_p \left(\frac{\partial T}{\partial t} + \tilde{\mathbf{v}}(x, t) \cdot \nabla T \right) - \nabla \cdot (\mathbf{k} \nabla T) = 0, \quad t \in \mathcal{T}, x \in \Omega \quad (1a)$$

$$-\mathbf{k} \nabla T \cdot \mathbf{n} = q_b(x, t), \quad t \in \mathcal{T}, x \in \Gamma_q \quad (1b)$$

$$T(x, t) = T_b(x, t), \quad t \in \mathcal{T}, x \in \Gamma_T \quad (1c)$$

$$T(x, 0) = T_0(x), \quad x \in \Omega \quad (1d)$$

¹³⁰ where ρ , c_p , and $\mathbf{k} \in \mathbb{R}^{d \times d}$ are the constant density, heat capacity, and thermal conductivity, respectively. Note that our prior work has applied the PIROM to TPS problems ¹³¹ with temperature-varying material properties [18]. In Eq. (1) the $\rho c_p \frac{\partial T}{\partial t}$ term includes the ¹³² unsteady energy storage, $\rho c_p \tilde{\mathbf{v}}(x, t) \cdot \nabla T$ includes the temperature advection due to ablation, ¹³³ and $\nabla \cdot (\mathbf{k} \nabla T)$ includes the heat conduction. ¹³⁴

¹³⁵ An Arbitrary Lagrangian-Eulerian (ALE) description is used to account for mesh motion ¹³⁶ due to surface recession. The relative velocity of the material $\tilde{\mathbf{v}}(x, t)$ with respect to the ¹³⁷ mesh is,

$$\tilde{\mathbf{v}}(x, t) = \mathbf{v}_s(x, t) - \mathbf{v}_m(x, t) \quad (2)$$

¹³⁸ where $\mathbf{v}_s(x, t)$ and $\mathbf{v}_m(x, t)$ are the physical material velocity and mesh velocity, respectively. ¹³⁹ In this work, the physical material velocity is assumed to be zero, i.e., $\mathbf{v}_s(x, t) = \mathbf{0}$, and thus ¹⁴⁰ the relative velocity is simply the negative of the mesh velocity, $\tilde{\mathbf{v}}(x, t) = -\mathbf{v}_m(x, t)$. The ¹⁴¹ advection term in Eq. (1a) thus captures the effect of temperature advection due to mesh ¹⁴² motion, and the governing equation for the mesh velocity is provided next.

¹⁴³ 2.1.2 Pseudo-Elasticity Equation

¹⁴⁴ At some time t , the mesh displacement field $\mathbf{d}_m \in \mathbb{R}^d$ is described by the steady-state ¹⁴⁵ pseudo-elasticity equation, which models the mesh as a fictitious elastic solid that deforms ¹⁴⁶ according to the prescribed boundary displacements. The mesh velocities are obtained by ¹⁴⁷ differentiating the mesh displacements with respect to time, i.e., $\mathbf{v}_m(x, t) = \dot{\mathbf{d}}_m$, which appear ¹⁴⁸ in the advection term of the energy equation in Eq. (1a) and is approximated using finite ¹⁴⁹ differences in the coupled simulation. The governing equation for mesh displacements is,

$$\nabla \cdot \boldsymbol{\sigma}(\mathbf{d}_m) = \mathbf{0}, \quad \forall x \in \Omega \quad (3a)$$

$$\mathbf{d}_m(x, t) = \mathbf{d}_q(x, t), \quad \forall x \in \Gamma_q \quad (3b)$$

$$\mathbf{d}_m(x, t) = \mathbf{0}, \quad \forall x \in \Gamma_T \quad (3c)$$

$$\mathbf{d}_m(x, 0) = \mathbf{0}, \quad \forall x \in \Omega \quad (3d)$$

¹⁵⁰ where the stress tensor $\boldsymbol{\sigma}$ is related to the strain tensor $\boldsymbol{\epsilon}(\mathbf{d}_m)$ through Hooke's law,

$$\boldsymbol{\sigma}(\mathbf{d}_m) = \mathbb{D} : \boldsymbol{\epsilon}(\mathbf{d}_m)$$

¹⁵¹ where \mathbb{D} is the fourth-order positive definite elasticity tensor, and ":" is the double contrac- ¹⁵² tion of the full-order tensor \mathbb{D} with the second-order tensor $\boldsymbol{\epsilon}$. In this work, the standard ¹⁵³ isotropic case is considered, where \mathbb{D} is fully described by two Lamé parameters λ and μ

154 arbitrarily. The symmetric strain tensor $\boldsymbol{\epsilon}$ measures the deformation of the mesh due to
155 displacements $\mathbf{d}_m(x, t)$, and is defined as,

$$\boldsymbol{\epsilon}(\mathbf{d}_m) = \frac{1}{2} (\nabla \mathbf{d}_m + \nabla \mathbf{d}_m^\top)$$

156 The “material” properties for the mesh are chosen to tailor the mesh deformation, and need
157 not represent the actual material being modeled [1].

158 The boundary conditions \mathbf{d}_q and $\mathbf{d}_T = \mathbf{0}$ are Dirichlet-type on the heated Γ_q and unheated
159 Γ_T boundaries, respectively, and the initial mesh displacement is set to zero as in Eq. (3d).
160 The surface velocity due to ablation is a function of the surface temperature $T_q(x, t)$ for
161 $x \in \Gamma_q$. For the i -th material component, the mesh velocity is imposed based on the following
162 relation,

$$\hat{\mathbf{n}} \cdot \mathbf{v}_m(x, t) = f_i(T_q(x, t)), \quad x \in \Gamma_{q,i} \quad (4)$$

163 where $\Gamma_q = \cup_{i=1}^{\tilde{N}} \Gamma_{q,i}$ with $\Gamma_{q,i}$ as the portion of the heated boundary that belongs to the
164 i -th ablative component, \tilde{N} is the number of ablative components with $\tilde{N} \leq N$, $\hat{\mathbf{n}}$ is the
165 unit normal vector, and f_i is a material-dependent function obtained from tabulated data,
166 commonly referred to as a B' table [1]. The B' table provides a model for the recession
167 velocity as a function of the surface temperature, and is pre-computed based on high-fidelity
168 simulations or physical experiments for a one-dimensional slab of materials, and is indepen-
169 dent of the TPS geometry. Provided the surface velocity, the boundary condition in Eq. (5)
170 for the mesh displacements are computed by integrating the surface velocity over time,

$$\mathbf{d}_q(x, t) = \int_0^t \mathbf{v}_m(x, \tau) d\tau, \quad x \in \Gamma_q \quad (5)$$

171 2.2 Full-Order Model: Finite-Element Method

172 The transient thermo-ablative response of the TPS is modeled using a high-fidelity FOM
173 based on FEM. The governing PDEs – namely, the energy equation in Eq. (1) and the
174 pseudo-elasticity equation in Eq. (3) – are spatially discretized using the Aria multi-physics
175 code developed at Sandia National Laboratories [2]. A *Discontinuous Galerkin FEM* (DG-
176 FEM) method is used to spatially discretize the energy equation for theoretical convenience
177 in the subsequent PIROM derivation, while a standard Galerkin FEM is used to spatially
178 discretize the pseudo-elasticity equation for mesh motion. The following discussion presents
179 the spatial discretization of both governing equations.

180 **Energy Equation** To obtain the full-order numerical solution, the *energy equation* is spa-
181 tially discretized using variational principles of DG-FEM [5]. Note that the choice of DG
182 approach is mainly for theoretical convenience, and is exclusively performed on the energy
183 equation, as it is the surface temperature that drives the ablation process; the equivalence be-
184 tween DG and FEM is noted upon their convergence. Consider a conforming mesh partition
185 domain, where each element belongs to one and only one component. Denote the collection
186 of all M elements as $\{E_i\}_{i=1}^M$. In an element E_i , its shared boundaries with another element
187 E_j , Neumann BC, and Dirichlet BC are denoted as e_{ij} , e_{iq} , and e_{iT} , respectively. Lastly,

¹⁸⁸ $|e|$ denotes the length ($n_d = 2$) or area ($n_d = 3$) of a component boundary e . For the i -th
¹⁸⁹ element, use a set of P trial functions, such as polynomials, to represent the temperature
¹⁹⁰ distribution,

$$T_i(x, t) = \sum_{l=1}^P \phi_l^i(x) u_l^i(t) \equiv \boldsymbol{\phi}_i^\top(x) \mathbf{u}_i(t), \quad i = 1, 2, \dots, M \quad (6)$$

¹⁹¹ Then, the energy equation is collected into a block-system of ODEs for all the elements in
¹⁹² the mesh,

$$\mathbf{A}\dot{\mathbf{u}} = [\mathbf{B} + \mathbf{C}(\mathbf{u})] \mathbf{u} + \mathbf{f}(t) \quad (7)$$

¹⁹³ where $\mathbf{u} = [\mathbf{u}_1, \mathbf{u}_2, \dots, \mathbf{u}_M]^\top \in \mathbb{R}^{MP}$ includes all the DG variables, $\mathbf{f} \in \mathbb{R}^{MP}$ is the external
¹⁹⁴ forcing, and the system matrices \mathbf{A} , \mathbf{B} , and \mathbf{C} are the matrices due to heat capacity, heat
¹⁹⁵ conduction, and temperature advection due to mesh motion, respectively. Note that the
¹⁹⁶ advection matrix $\mathbf{C}(\mathbf{u})$ is a function of the mesh velocity \mathbf{v}_m , which in turn is a function
¹⁹⁷ of temperature through the boundary condition in Eq. (4).; this is the main source of non-
¹⁹⁸ linearity in the current TPS problem. A detailed derivation of Eq. (7) and their matrices is
¹⁹⁹ provided in Appendix A.

²⁰⁰ **Pseudo-Elasticity Equation** The *pseudo-elasticity equation* is spatially discretized us-
²⁰¹ ing the standard Galerkin FEM method on a structured mesh with quadrilateral elements.
²⁰² Define the scalar basis functions $\{\psi_q(x)\}_{q=1}^Q$ nodal variables $\{\mathbf{d}_q\}_{q=1}^Q$ for the mesh displace-
²⁰³ ments, where Q is the number of basis functions. Express the mesh displacements \mathbf{d} at time
²⁰⁴ t as,

$$\mathbf{d}(x, t) \approx \sum_{q=1}^Q \psi_q(x) \mathbf{d}_q \quad (8)$$

²⁰⁵ Substituting into the variational form the *steady* pseudo-elasticity equation, the following
²⁰⁶ linear system of equations is obtained for the nodal displacements at each time step,

$$\mathbf{K}\mathbf{d} = \mathbf{g} \quad (9)$$

²⁰⁷ where \mathbf{d} is the global displacement vector, $\mathbf{K} \in \mathbb{R}^{dQ \times dQ}$ the global stiffness matrix of dimen-
²⁰⁸ sion d , defined by the volume integrals over the domain Ω provided the elasticity tensor \mathbb{D} ,
²⁰⁹ and \mathbf{g} is the global force vector due to the Dirichlet boundary conditions on the heated Γ_q
²¹⁰ and unheated Γ_T boundaries.

²¹¹ **Coupled Full-Order Model** The temperature-dependent mesh motion on the heated
²¹² boundary Γ_q naturally defines a two-way coupling scheme between the energy and pseudo-
²¹³ elasticity FEM models. At each time step, the mesh displacements \mathbf{d}_m are obtained by
²¹⁴ solving Eq. (9), where the Dirichlet boundary conditions on Γ_q are computed by integrating
²¹⁵ the surface recession velocity provided by the surface temperature from the energy equation.
²¹⁶ Then, the mesh velocity $\dot{\mathbf{d}}_m = \mathbf{v}_m$ is computed using finite differences, which is used as an
²¹⁷ input into the advection matrix $\mathbf{C}(\mathbf{u})$ in Eq. (7). Finally, the temperature field is advanced
²¹⁸ in time for the next time step using Eq. (7) based on an implicit time-integration scheme.
²¹⁹ This procedure is repeated until the final time t_f is reached.

220 **2.3 Reduced-Physics Model**

221 The RPM for predicting the response of the ablating TPS consists of two components: (1)
 222 *surface recession model* (SRM) and a *lumped capacitance model* (LCM). The SRM provides
 223 a relation between the surface temperature and *one-dimensional* surface recession veloc-
 224 ity based on pre-computed B' tables for the material, enabling the computation of *one-*
 225 *dimensional* surface displacements. Provided the geometry changed induced by the surface
 226 recession, the LCM predicts the average temperature inside each component of the TPS,
 227 which are in turn used as low-fidelity estimates for the surface temperatures required by the
 228 SRM. Therefore, the SRM and LCM are coupled to define the RPM, providing low-fidelity
 229 estimates for temperatures and surface recessions of the ablating TPS.

230 **2.3.1 Surface Recession Model**

231 The mesh displacements \mathbf{d} are constrained to be *one-dimensional* on the heated boundary
 232 Γ_q , i.e., $w_i(x, t) = \mathbf{d}(x, t) \cdot \hat{\mathbf{n}}_i$, where $\hat{\mathbf{n}}_i$ is the unit normal vector on the heated boundary
 233 $\Gamma_{q,i}$. Displacements perpendicular to $\hat{\mathbf{n}}_i$ for $i = 1, \dots, \tilde{N}$ are assumed to be small and thus
 234 neglected. Let $\mathbf{w} = [w_1, w_2, \dots, w_{\tilde{N}}]^\top \in \mathbb{R}^{\tilde{N}}$ include the one-dimensional displacements for
 235 the \tilde{N} ablating components on the heated boundary, where $\tilde{N} \leq N$. Then the SRM is
 236 described as,

$$\dot{\mathbf{w}} = \boldsymbol{\Xi}\mathbf{u} - \tilde{\mathbf{f}} \quad (10)$$

237 where $\boldsymbol{\Xi} = \text{diag}(\alpha_1, \dots, \alpha_{\tilde{N}})$ and $\tilde{\mathbf{f}} = (\alpha_1 u_{0,1}, \dots, \alpha_{\tilde{N}} u_{0,\tilde{N}})^\top$. The constants α_i are small
 238 material-dependent parameters, determined from the B' table, and $u_{0,i}$ is the constant initial
 239 temperature of the ablative component. The SRM provides a relation between the surface's
 240 temperature and recession velocity, based on pre-computed B' tables for the material.

241 **2.3.2 Lumped Capacitance Model**

242 A general form of the LCM is provided in this section; details regarding the derivation for
 243 the four-component TPS used in the results section are provided in Appendix A. Let Ω be
 244 partitioned into N non-overlapping components $\{\Omega_i\}_{i=1}^N$, as illustrated in Fig. 2 for $N = 2$.
 245 The domain Ω is a function of the surface displacements \mathbf{w} , and thus the geometry of each
 246 component Ω_i is time-dependent. The LCM predicts the temporal variation of average
 247 temperatures in multiple shape-varying interconnected components [9]. From a point of
 248 view of energy conservation, the LCM leads to the following system of first-order ODEs for
 249 the average temperatures in the components,

$$\bar{\mathbf{A}}(\mathbf{w})\dot{\bar{\mathbf{u}}} = \bar{\mathbf{B}}(\mathbf{w})\bar{\mathbf{u}} + \bar{\mathbf{f}}(t) \quad (11)$$

250 Where the states and inputs,

$$\bar{\mathbf{u}} = [\bar{u}_1, \bar{u}_2, \dots, \bar{u}_N]^\top \in \mathbb{R}^N, \quad \bar{\mathbf{f}} = [\bar{f}_1, \bar{f}_2, \dots, \bar{f}_N]^\top \in \mathbb{R}^N \quad (12)$$

251 include the average temperatures $\bar{\mathbf{u}}$ and spatially-integrated inputs $\bar{\mathbf{f}}$ for the N components.
 252 For $i, j = 1, 2, \dots, N$ the (i, j) -th elements of the $\bar{\mathbf{A}} \in \mathbb{R}^{N \times N}$, $\bar{\mathbf{B}} \in \mathbb{R}^{N \times N}$, and $\bar{\mathbf{f}} \in \mathbb{R}^N$

253 matrices are given by,

$$\bar{A}_i = \begin{cases} \int_{\Omega_i} \rho c_p d\Omega_i, & i = j \\ 0, & i \neq j \end{cases}, \quad \bar{B}_{ij} = \begin{cases} \sum_{j \in \mathcal{N}_i \cup \{T_b\}} \bar{B}_{ij}^i, & i = j \\ \bar{B}_{ij}^{(j)}, & i \neq j \end{cases}, \quad (13a)$$

$$\mathbf{f}_i = \begin{cases} |e_{iq}| \bar{q}_i + \frac{|e_{iT}|}{R_i} \bar{T}_i, & i = j \\ 0, & i \neq j \end{cases} \quad (13b)$$

254 where,

$$\bar{q}_i = \frac{1}{|e_{iq}|} \int_{e_{iq}} q_b d e_{iq}, \quad \bar{T}_i = \frac{1}{|e_{iT}|} \int_{e_{iT}} T_b d e_{iT}, \quad \bar{B}_{ij}^i = -\frac{|e_{ij}|}{R_{ij}}, \quad \bar{B}_{ij}^j = \frac{|e_{ij}|}{R_{ij}} \quad (14)$$

255 where R_{ij} is the equivalent thermal resistance between two neighboring components Ω_i and
256 Ω_j , and R_i is the thermal resistance between component Ω_i and the Dirichlet boundary.
257 Note that the heat capacitances and thermal resistances are computed based on the current
258 geometry of each component, which is a function of \mathbf{w} provided by the SRM.

259 2.3.3 Thermo-Ablative Reduced-Physics Model

260 The SRM and LCM are combined to define the RPM for predicting the thermo-ablative
261 response of the TPS under hypersonic boundary layers. Specifically, the RPM is defined as
262 the LCM as in Eq. (11), where the *geometry-dependent* matrices $\bar{\mathbf{A}}$ and $\bar{\mathbf{B}}$ are updated at
263 each time step based on the current displacements \mathbf{w} provided by the SRM. The RPM is
264 formally stated as,

$$\tilde{\mathbf{A}}(\mathbf{s})\dot{\mathbf{s}} = \tilde{\mathbf{B}}(\mathbf{s})\mathbf{s} + \tilde{\mathbf{F}}(t) \quad (15a)$$

$$\tilde{\mathbf{z}} = \mathbf{s} \quad (15b)$$

265 where the state $\mathbf{s} = [\bar{\mathbf{u}}, \mathbf{w}]^\top \in \mathbb{R}^{N+\tilde{N}}$ includes the *average temperature* and *one-dimensional*
266 *surface displacements*, and \tilde{N} is the number of ablating components with $\tilde{N} \leq N$. Moreover,
267 the observables are defined as $\mathbf{z} = [\bar{\mathbf{u}}, \mathbf{w}]^\top \in \mathbb{R}^{N+\tilde{N}}$. The matrices are given as,

$$\tilde{\mathbf{A}}(\mathbf{s}) = \begin{bmatrix} \bar{\mathbf{A}}(\mathbf{s}) & \mathbf{0} \\ \mathbf{0} & \mathbf{I} \end{bmatrix}, \quad \tilde{\mathbf{B}}(\mathbf{s}) = \begin{bmatrix} \bar{\mathbf{B}}(\mathbf{s}) & \mathbf{0} \\ \Xi & \mathbf{0} \end{bmatrix}, \quad \tilde{\mathbf{F}}(t) = \begin{bmatrix} \bar{\mathbf{f}}(t) \\ -\tilde{\mathbf{f}} \end{bmatrix} \quad (16)$$

268 In the matrices $\tilde{\mathbf{A}}$ and $\tilde{\mathbf{B}}$, the surface displacements \mathbf{w} are used to define the dimensions for
269 the Ω_i component used in Eqs. (13) and (14), thus effectively coupling the LCM and SRM.

270 2.4 Summary of Modeling Approaches

271 The FOM (i.e., FEM) and RPM (i.e., LCM with SRM) are two different but mathematically
272 connected solution strategies. Particularly, the LCM in Eq. (11) not only resembles the
273 functional form of the DG model in Eq. (7), but can be viewed as a special case of the latter,
274 where the mesh partition is extremely coarse, and the trial and test functions are piece-wise

275 constants. This removes all spatial variations within each component, and neglects advection
276 effects due to mesh motion.

277 For example, consider the case where each component Ω_i is treated as one single element,
278 and each element employs one constant basis function $\phi_i = 1$. The DG-FEM model for the
279 i -th component simplifies to the scalar ODE,

$$\mathbf{A}^i = \bar{A}_i, \quad \mathbf{C}^i = 0, \quad \mathbf{B}_{ij}^i = -\sigma|e_{ij}|, \quad \mathbf{B}_{ij}^j = \sigma|e_{ij}|, \quad \mathbf{f}_i = |e_{iq}|\bar{q}_i + \sigma|e_{iT}|\bar{T}_i \quad (17)$$

280 Clearly, the LCM is a coarse zeroth-order DG model with the inverse of thermal resistance
281 chosen as the element-wise penalty factors. Or conversely, the DG model is a refined version
282 of LCM via hp -adaptation.

283 The FOM and RPM represent two extremes in the modeling fidelity and computational
284 cost spectrum. On one hand, the FOM is the most accurate but computationally expensive
285 to evaluate due to the fine mesh discretizations for both the temperature and displacement
286 fields, leading to possibly millions of state variables. On the other hand, the RPM considers
287 only the average temperature of the material, from which the displacements are obtained by
288 integrating the velocity. The coarsened representation of the temperature field significantly
289 reduces the number of state variables to only a few per component, and thus reducing the
290 computational cost. However, this sacrifices local temperature information that becomes
291 critical to properly capture higher-order effects due to mesh motion and thermal gradients
292 within each component. Thus, neither the FOM nor the RPM is an universal approach for
293 real-world analysis, design, and optimization tasks for ablating TPS, where thousands of
294 high-fidelity model evaluations may be necessary. This issue motivates the development of
295 the PIROM, which can achieve the fidelity of FOM at a computational cost close to the
296 RPM, while maintaining the generalizability to model parameters.

297 3 Physics-Infused Reduced-Order Modeling

298 The formulation of PIROM for ablating TPS starts by connecting the FOM, i.e., the DG-
299 FEM, and the RPM, i.e., the LCM, via a coarse-graining procedure. This procedure pin-
300 points the missing dynamics in the LCM when compared to DG-FEM. Subsequently, the
301 Mori-Zwanzig (MZ) formalism is employed to determine the model form for the missing dy-
302 namics in PIROM. Lastly, the data-driven identification of the missing dynamics in PIROM
303 is presented.

304 3.1 Deriving the Reduced-Physics Model via Coarse-Graining

305 The subsequent coarse-graining formulation is performed on the DG-FEM in Eq. (7) to
306 derive the LCM in Eq. (11). This process constraints the trial function space of a full-
307 order DG model to a subset of piece-wise constants, so that the variables \mathbf{u} , matrices \mathbf{A} ,
308 \mathbf{B} , and \mathbf{C} , and forcing vector \mathbf{f} are all approximated using a single state associated to the
309 average temperature. Note that the coarse-graining is exclusively performed on the thermal
310 dynamics, as it is the surface temperature that drives the one-dimensional recession via
311 the SRM. Hence, the coarse-graining of the mesh dynamics is not included in the following

³¹² procedure.

³¹³ 3.1.1 Coarse-Graining of States

³¹⁴ Consider a DG model as in Eq. (7) for M elements and an LCM as in Eq. (11) for N
³¹⁵ components; clearly $M \gg N$. Let $\mathcal{V}_j = \{i | E_i \in \Omega_j\}$ be the indices of the elements belonging
³¹⁶ to the j -th component, so $E_i \in \Omega_j$ for all $i \in \mathcal{V}_j$. The number of elements in the j -th
³¹⁷ component is $|\mathcal{V}_j|$. The average temperature on Ω_j is,

$$\bar{u}_j = \frac{1}{|\Omega_j|} \sum_{i \in \mathcal{V}_j} \int_{E_i} \phi^{(i)}(x)^T \mathbf{u}^{(i)} d\Omega = \frac{1}{|\Omega_j|} \sum_{i \in \mathcal{V}_j} |E_i| \boldsymbol{\varphi}_i^{j\top} \mathbf{u}^{(i)}, \quad j = 1, 2, \dots, N \quad (18)$$

³¹⁸ where $|\Omega_j|$ and $|E_i|$ denote the area ($d = 2$) or volume ($d = 3$) of component j and element
³¹⁹ i , respectively. The orthogonal basis functions are defined as $\boldsymbol{\varphi}_i^{j\top} = [1, 0, \dots, 0]^\top \in \mathbb{R}^P$.

³²⁰ Conversely, given the average temperatures of the N components, $\bar{\mathbf{u}}$, the states of an
³²¹ arbitrary element E_i is written as,

$$\mathbf{u}^{(i)} = \sum_{k=1}^N \boldsymbol{\varphi}_i^k \bar{u}_k + \delta \mathbf{u}^{(i)}, \quad i = 1, 2, \dots, M \quad (19)$$

³²² where $\boldsymbol{\varphi}_i^k = 0$ if $i \notin \mathcal{V}_k$, and $\delta \mathbf{u}^{(i)}$ represents the deviation from the average temperature and
³²³ satisfies the orthogonality condition $\boldsymbol{\varphi}_i^{k\top} \delta \mathbf{u}^{(i)} = 0$ for all k .

³²⁴ Equations Eqs. (18) and (19) are combined and written in matrix form as,

$$\bar{\mathbf{u}} = \boldsymbol{\Phi}^+ \mathbf{u}, \quad \mathbf{u} = \boldsymbol{\Phi} \mathbf{u} + \delta \mathbf{u} \quad (20)$$

³²⁵ where $\boldsymbol{\Phi} \in \mathbb{R}^{MP \times N}$ is a matrix of $M \times N$ blocks, with the (i, j) -th block as $\boldsymbol{\varphi}_i^j$, $\boldsymbol{\Phi}^+ \in \mathbb{R}^{N \times MP}$
³²⁶ is the left inverse of $\boldsymbol{\Phi}$, with the (i, j) -th block as $\boldsymbol{\varphi}_i^{j+} = \frac{|E_i|}{|\Omega_j|} \boldsymbol{\varphi}_i^{j\top}$, and $\delta \mathbf{u}$ is the collection of
³²⁷ deviations. By their definitions, $\boldsymbol{\Phi}^+ \boldsymbol{\Phi} = \mathbf{I}$ and $\boldsymbol{\Phi}^+ \delta \mathbf{u} = \mathbf{0}$.

³²⁸ 3.1.2 Coarse-Graining of Dynamics

³²⁹ The dependence of the matrices with respect to the displacements \mathbf{w} is dropped to isolate
³³⁰ the analysis based on coarsened variables. Consider a function of states in the form of
³³¹ $\mathbf{M}(\mathbf{u}) \mathbf{g}(\mathbf{u})$, where $\mathbf{g} : \mathbb{R}^{MP} \rightarrow \mathbb{R}^{MP}$ is a vector-valued function, and $\mathbf{M} : \mathbb{R}^{MP} \rightarrow \mathbb{R}^{p \times MP}$
³³² is a matrix-valued function with an arbitrary dimension p . Define the projection matrix
³³³ $\mathbf{P} = \boldsymbol{\Phi} \boldsymbol{\Phi}^+$ and the projection operator \mathcal{P} as,

$$\begin{aligned} \mathcal{P} [\mathbf{M}(\mathbf{u}) \mathbf{g}(\mathbf{u})] &= \mathbf{M}(\mathbf{P} \mathbf{u}) \mathbf{g}(\mathbf{P} \mathbf{u}) \\ &= \mathbf{M}(\boldsymbol{\Phi} \bar{\mathbf{u}}) \mathbf{g}(\boldsymbol{\Phi} \bar{\mathbf{u}}) \end{aligned} \quad (21)$$

³³⁴ so that the resulting function depends only on the average temperatures $\bar{\mathbf{u}}$. Correspondingly,
³³⁵ the residual operator $\mathcal{Q} = \mathcal{I} - \mathcal{P}$, and $\mathcal{Q} [\mathbf{M}(\mathbf{u}) \mathbf{g}(\mathbf{u})] = \mathbf{M}(\mathbf{u}) \mathbf{g}(\mathbf{u}) - \mathbf{M}(\boldsymbol{\Phi} \bar{\mathbf{u}}) \mathbf{g}(\boldsymbol{\Phi} \bar{\mathbf{u}})$. When
³³⁶ the function is not separable, the projection operator is simply defined as $\mathcal{P} [\mathbf{g}(\mathbf{u})] = \mathbf{g}(\mathbf{P} \mathbf{u})$.

³³⁷ Subsequently, the operators defined above are applied to coarse-grain the dynamics. First,
³³⁸ write the DG-FEM in Eq. (7) as,

$$\dot{\mathbf{u}} = \mathbf{A}^{-1}\mathbf{B}\mathbf{u} + \mathbf{A}^{-1}\mathbf{C}(\mathbf{u})\mathbf{u} + \mathbf{A}^{-1}\mathbf{f}(t) \quad (22)$$

³³⁹ and multiply both sides by Φ^+ to obtain,

$$\Phi^+\dot{\mathbf{u}} = \Phi^+(\Phi\dot{\mathbf{u}} + \delta\dot{\mathbf{u}}) = \dot{\bar{\mathbf{u}}} = \Phi^+\mathbf{r}(\mathbf{u}, t) \quad (23)$$

³⁴⁰ Apply the projection operator \mathcal{P} and the residual operator \mathcal{Q} to the right-hand side to obtain,

$$\dot{\bar{\mathbf{u}}} = \mathcal{P}[\Phi^+\mathbf{r}(\mathbf{u}, t)] + \mathcal{Q}[\Phi^+\mathbf{r}(\mathbf{u}, t)] \equiv \mathbf{r}^{(1)}(\bar{\mathbf{u}}, t) + \mathbf{r}^{(2)}(\mathbf{u}, t) \quad (24)$$

³⁴¹ where $\mathbf{r}^{(1)}(\bar{\mathbf{u}}, t)$ is resolved dynamics that depends on $\bar{\mathbf{u}}$ only, and $\mathbf{r}^{(2)}(\mathbf{u}, t)$ is the un-resolved
³⁴² or residual dynamics. Detailed derivations and analysis of $\mathbf{r}^{(1)}(\bar{\mathbf{u}}, t)$ and $\mathbf{r}^{(2)}(\mathbf{u}, t)$ can be
³⁴³ found in the Appendix.

³⁴⁴ It follows from our previous work in Ref. [18] that the resolved dynamics is exactly the
³⁴⁵ LCM, where the advection term reduces to zero, i.e., $\bar{\mathbf{C}}(\bar{\mathbf{u}}) = \mathbf{0}$, as shown in the Appendix.
³⁴⁶ Using the notation from Eq. (11), it follows that,

$$\begin{aligned} \mathbf{r}^{(1)}(\bar{\mathbf{u}}, t) &= \bar{\mathbf{A}}(\mathbf{w})^{-1}\bar{\mathbf{B}}(\mathbf{w})\bar{\mathbf{u}} + \bar{\mathbf{A}}(\mathbf{w})^{-1}\bar{\mathbf{C}}(\bar{\mathbf{u}})\bar{\mathbf{u}} + \bar{\mathbf{A}}(\mathbf{w})^{-1}\bar{\mathbf{f}}(\bar{\mathbf{u}}) \\ &= \bar{\mathbf{A}}(\mathbf{w})^{-1}\bar{\mathbf{B}}(\mathbf{w})\bar{\mathbf{u}} + \bar{\mathbf{A}}(\mathbf{w})^{-1}\bar{\mathbf{f}}(t) \end{aligned} \quad (25)$$

³⁴⁷ where the following relations hold,

$$\bar{\mathbf{A}}(\mathbf{w}) = \mathbf{W}(\Phi^+\mathbf{A}^{-1}\Phi)^{-1} \quad (26a)$$

$$\bar{\mathbf{B}}(\mathbf{w}) = \mathbf{W}\Phi^+\mathbf{B}\Phi \quad (26b)$$

³⁴⁸ where $\mathbf{W} \in \mathbb{R}^{N \times N}$ is a diagonal matrix with the i -th element as $[\mathbf{W}]_{ii} = |\mathcal{V}_k|$ if $i \in \mathcal{V}_k$.
³⁴⁹ The examination of the second residual term $\mathbf{r}^{(2)}(\mathbf{u}, t)$ in Eq. (24) is shown in the Appendix,
³⁵⁰ and demonstrates that the physical sources of missing dynamics in the LCM include: the
³⁵¹ approximation of non-uniform temperature within each component as a constant, and the
³⁵² elimination of the advection term due to coarse-graining. In sum, the above along with the
³⁵³ derivations in the Appendix not only show that the LCM is a result of coarse-graining of
³⁵⁴ the full-order DG-FEM, but also reveal the discrepancies between the LCM and the DG-
³⁵⁵ FEM. These discrepancies propagate into the SRM, which as a result of the averaging in the
³⁵⁶ LCM formulation, under-predicts the surface recession rates. In the subsequent section, the
³⁵⁷ discrepancies in the LCM are corrected to formulate the PIROM.

³⁵⁸ 3.2 Physics-Infusion Via Mori-Zwanzig Formalism

³⁵⁹ The Mori-Zwanzig (MZ) formalism is an operator-projection technique used to derive ROMs
³⁶⁰ for high-dimensional dynamical systems, especially in statistical mechanics and fluid dy-
³⁶¹ namics [13, 14, 15]. It provides an exact reformulation of a high-dimensional Markovian dy-
³⁶² namical system, into a low-dimensional observable non-Markovian dynamical system. The
³⁶³ proposed ROM is subsequently developed based on the approximation to the non-Markovian

term in the observable dynamics. Particularly, Eq. (24) shows that the DG-FEM dynamics can be decomposed into the resolved dynamics $\mathbf{r}^{(1)}(\bar{\mathbf{u}}, t)$ and the orthogonal dynamics $\mathbf{r}^{(2)}(\mathbf{u}, t)$, in the sense of $\mathcal{P}\mathbf{r}^{(2)} = 0$. In this case, the MZ formalism can be invoked to express the dynamics $\bar{\mathbf{u}}$ in terms of $\bar{\mathbf{u}}$ alone as the projected Generalized Langevin Equation (GLE) [13, 14, 15],

$$\dot{\bar{\mathbf{u}}}(t) = \mathbf{r}^{(1)}(\bar{\mathbf{u}}, t) + \int_0^t \tilde{\boldsymbol{\kappa}}(t, s, \bar{\mathbf{u}}) ds \quad (27)$$

where the first and second terms are referred to as the Markovian and non-Markovian terms, respectively. The non-Markovian term accounts for the effects of past un-resolved states on the current resolved states via a memory kernel $\tilde{\boldsymbol{\kappa}}(t, s, \bar{\mathbf{u}})$, which in practice is computationally expensive to evaluate.

3.2.1 Markovian Reformulation

This section details the formal derivation of the PIROM as a system of ODEs for the thermal dynamics, based on approximations to the memory kernel. Specifically, the kernel $\tilde{\mathbf{k}}$ is examined via a leading-order expansion, based on prior work [20]; this can be viewed as an analog of zeroth-order holding in linear system theory with a sufficiently small time step. In this case, the memory kernel is approximated as,

$$\tilde{\boldsymbol{\kappa}}(t, s, \bar{\mathbf{u}}) \approx \mathbf{r}^{(1)}(\bar{\mathbf{u}}, t) \cdot \nabla_{\bar{\mathbf{u}}} \mathbf{r}^{(2)}(\Phi \bar{\mathbf{u}}, t) \quad (28)$$

Note that the terms in $\mathbf{r}^{(1)}$ have a common factor $\bar{\mathbf{A}}^{-1}$; this motivates the following heuristic modification of the model form in Eq. (27),

$$\dot{\bar{\mathbf{u}}} = \mathbf{r}^{(1)}(\bar{\mathbf{u}}, t) + \bar{\mathbf{A}}(\mathbf{w})^{-1} \int_0^t \boldsymbol{\kappa}(t, s, \bar{\mathbf{u}}) ds \quad (29a)$$

$$\bar{\mathbf{A}}(\mathbf{w}) \dot{\bar{\mathbf{u}}} = \bar{\mathbf{B}}(\mathbf{w}) \bar{\mathbf{u}} + \bar{\mathbf{f}}(t) + \int_0^t \boldsymbol{\kappa}(t, s, \bar{\mathbf{u}}) ds \quad (29b)$$

where the original kernel $\tilde{\boldsymbol{\kappa}}$ is effectively normalized by $\bar{\mathbf{A}}(\mathbf{w})^{-1}$. Intuitively, such choice of kernel reduces its dependency on the averaged material properties, and simplifies the subsequent design of model form.

Subsequently, the hidden states are introduced to “Markovianize” the system Eq. (27). In this manner, Eq. (29b) is converted into a pure state-space model, with the functional form of the LCM retained; since LCM is a physics-based model, then it encodes the physical information and retains explicit parametric dependence of the problem. Consider the representation of the kernel as a finite sum of simpler functions, e.g., exponentials,

$$\boldsymbol{\kappa}(t, s, \bar{\mathbf{u}}) = \sum_{j=1}^m \mathcal{K}_j(t, s, \bar{\mathbf{u}}) [\mathbf{p}_j + \mathbf{d}_j(\bar{\mathbf{u}})] \phi_j(s, \bar{\mathbf{u}}) \quad (30)$$

where,

$$\mathcal{K}_j(t, s, \bar{\mathbf{u}}) = e^{-\int_s^t (\lambda_j + e_j(\bar{\mathbf{u}})) d\tau}, \quad \phi_j(s, \bar{\mathbf{u}}) = \mathbf{q}_j^\top \bar{\mathbf{u}}(s) + \mathbf{g}_j(\bar{\mathbf{u}})^\top \bar{\mathbf{u}}(s) + \mathbf{r}_j^\top \bar{\mathbf{f}}(s) \quad (31)$$

³⁹⁰ with suitable coefficients $\mathbf{p}_j, \mathbf{d}_j, \mathbf{q}_j, \mathbf{g}_j, \mathbf{r}_j \in \mathbb{R}^N$ and decay rates $\lambda_j, e_j(\bar{\mathbf{u}}) > 0$, that need to
³⁹¹ be identified from data.

³⁹² Define the hidden states as,

$$\beta_j(t) = \int_0^t \mathcal{K}_j(s, \bar{\mathbf{u}}) \phi_j(s, \bar{\mathbf{u}}) ds \quad (32)$$

³⁹³ and differentiate with respect to time,,

$$\dot{\beta}_j(t) = -[\lambda_j + e_j(\bar{\mathbf{u}})] \beta_j(t) + \mathbf{q}_j^\top \bar{\mathbf{u}}(t) + \mathbf{g}_j(\bar{\mathbf{u}})^\top \bar{\mathbf{u}}(t) + \mathbf{r}_j^\top \bar{\mathbf{f}}(t) \quad (33)$$

³⁹⁴ to obtain the memory,

$$\int_0^t \boldsymbol{\kappa}(t, s, \bar{\mathbf{u}}) ds = \sum_{j=1}^m [\mathbf{p}_j + \mathbf{d}_j(\bar{\mathbf{u}})] \beta_j(t) \quad (34)$$

³⁹⁵ Then, Eq. (29b) is recast as the extended Markovian system,

$$\bar{\mathbf{A}}(\mathbf{w}) \dot{\bar{\mathbf{u}}} = \bar{\mathbf{B}}(\mathbf{w}) \bar{\mathbf{u}} + [\mathbf{P} + \mathbf{D}(\bar{\mathbf{u}})] \boldsymbol{\beta} + \bar{\mathbf{f}}(t) \quad (35a)$$

$$\dot{\boldsymbol{\beta}} = [\mathbf{Q} + \mathbf{G}(\bar{\mathbf{u}})] \bar{\mathbf{u}} + [\mathbf{E}(\bar{\mathbf{u}}) - \boldsymbol{\Lambda}] \boldsymbol{\beta} + \mathbf{R} \bar{\mathbf{f}}(t) \quad (35b)$$

³⁹⁶ where the data-driven operators associated to the hidden dynamics are collected as,

$$\boldsymbol{\Lambda} = \text{diag}[\lambda_1, \lambda_2, \dots, \lambda_m] \in \mathbb{R}^{m \times m}, \quad \mathbf{P} = [\mathbf{p}_1, \mathbf{p}_2, \dots, \mathbf{p}_m] \in \mathbb{R}^{N \times m} \quad (36a)$$

$$\mathbf{D}(\bar{\mathbf{u}}) = [\mathbf{d}_1(\bar{\mathbf{u}}), \mathbf{d}_2(\bar{\mathbf{u}}), \dots, \mathbf{d}_m(\bar{\mathbf{u}})] \in \mathbb{R}^{N \times m}, \quad \mathbf{Q} = [\mathbf{q}_1, \mathbf{q}_2, \dots, \mathbf{q}_m] \in \mathbb{R}^{m \times N} \quad (36b)$$

$$\mathbf{G}(\bar{\mathbf{u}}) = [\mathbf{g}_1(\bar{\mathbf{u}}), \mathbf{g}_2(\bar{\mathbf{u}}), \dots, \mathbf{g}_m(\bar{\mathbf{u}})] \in \mathbb{R}^{m \times N}, \quad \mathbf{R} = [\mathbf{r}_1, \mathbf{r}_2, \dots, \mathbf{r}_m] \in \mathbb{R}^{m \times N} \quad (36c)$$

$$\mathbf{E}(\bar{\mathbf{u}}) = \text{diag}[e_1(\bar{\mathbf{u}}), e_2(\bar{\mathbf{u}}), \dots, e_m(\bar{\mathbf{u}})] \in \mathbb{R}^{m \times m} \quad (36d)$$

³⁹⁷ The form of the temperature-dependent matrices $\mathbf{D}(\bar{\mathbf{u}})$, $\mathbf{G}(\bar{\mathbf{u}})$, and $\mathbf{E}(\bar{\mathbf{u}})$ is specified in the
³⁹⁸ next section. Since the hidden states $\boldsymbol{\beta}$ serve as the memory, their initial conditions are set
³⁹⁹ to zero, i.e., $\boldsymbol{\beta}(t_0) = \mathbf{0}$, no memory at the beginning. The physics-infused model in Eq. (35)
⁴⁰⁰ retains the structure of the LCM and depend on the displacements \mathbf{w} , while the hidden states
⁴⁰¹ account for missing physics through corrections to the stiffness and advection matrices, as
⁴⁰² well as the forcing term.

⁴⁰³ 3.2.2 Coupled Physics-Infused Model

⁴⁰⁴ The next step involves coupling the physics-infused model in Eq. (35) with the SRM in
⁴⁰⁵ Eq. (10) to define the PIROM for ablating TPS. To this end, define the surface temperature
⁴⁰⁶ $\mathbf{z}_u \in \mathbb{R}^{\tilde{N}}$ and displacements $\mathbf{z}_w \in \mathbb{R}^{\tilde{N}}$ for $\tilde{N} \leq N$ ablating components so that the observable
⁴⁰⁷ is given by $\mathbf{z} = [\mathbf{z}_u, \mathbf{z}_w]^\top \in \mathbb{R}^{n_z}$ with $n_z = 2\tilde{N}$ as the total number of observables.

⁴⁰⁸ Collect the RPM and hidden states into a single state vector $\mathbf{y} = [\bar{\mathbf{u}}, \mathbf{w}, \boldsymbol{\beta}]^\top \in \mathbb{R}^{n_y}$, where
⁴⁰⁹ $n_y = N + \tilde{N} + m$, and define a data-driven operator $\mathbf{M} \in \mathbb{R}^{n_z \times n_y}$ to define the PIROM's
⁴¹⁰ observable as,

$$\mathbf{z} = \mathbf{My} \quad (37)$$

411 where,

$$\mathbf{M} = \begin{bmatrix} \mathbf{M}_{\bar{u}} & \mathbf{0} & \mathbf{M}_{\beta} \\ \mathbf{0} & \mathbf{I} & \mathbf{0} \end{bmatrix} \quad (38)$$

412 includes the matrices $\mathbf{M}_{\bar{u}} \in \mathbb{R}^{\tilde{N} \times N}$ and $\mathbf{M}_{\beta} \in \mathbb{R}^{\tilde{N} \times m}$, which computes the surface tem-
413 perature observable from the RPM states and hidden states, respectively. The PIROM is
414 coupled to the SRM in Eq. (10) by leveraging Eq. (37) to compute the surface recession
415 velocity. Thus, the PIROM is formally stated as,

$$\mathcal{A}\dot{\mathbf{y}} = [\mathcal{B} + \mathcal{C}] \mathbf{y} + \mathcal{F}(t) \quad (39a)$$

$$\mathbf{z} = \mathbf{M}\mathbf{y} \quad (39b)$$

416 where,

$$\mathcal{A} = \begin{bmatrix} \bar{\mathbf{A}}(\mathbf{w}) & \mathbf{O} & \mathbf{O} \\ \mathbf{O} & \mathbf{I} & \mathbf{O} \\ \mathbf{O} & \mathbf{O} & \mathbf{I} \end{bmatrix} \in \mathbb{R}^{n_y \times n_y}, \quad \mathcal{B} = \begin{bmatrix} \bar{\mathbf{B}}(\mathbf{w}) & \mathbf{O} & \mathbf{P} \\ \Xi \mathbf{M}_u & \mathbf{O} & \Xi \mathbf{M}_{\beta} \\ \mathbf{Q} & \mathbf{O} & -\Lambda \end{bmatrix} \in \mathbb{R}^{n_y \times n_y}, \quad (40a)$$

$$\mathcal{C} = \begin{bmatrix} \mathbf{O} & \mathbf{O} & \mathbf{D}(\bar{\mathbf{u}}) \\ \mathbf{O} & \mathbf{O} & \mathbf{O} \\ \mathbf{G}(\bar{\mathbf{u}}) & \mathbf{O} & \mathbf{E}(\bar{\mathbf{u}}) \end{bmatrix} \in \mathbb{R}^{n_y \times n_y}, \quad \mathcal{F} = \begin{bmatrix} \bar{\mathbf{f}}(t) \\ -\tilde{\mathbf{f}} \\ \mathbf{R}\bar{\mathbf{f}}(t) \end{bmatrix} \in \mathbb{R}^{n_y} \quad (40b)$$

417 The learnable parameters in the PIROM are collected as,

$$\Theta = \{\mathbf{P}, \Lambda, \mathbf{Q}, \mathbf{M}, \mathbf{D}(\bar{\mathbf{u}}), \mathbf{G}(\bar{\mathbf{u}}), \mathbf{E}(\bar{\mathbf{u}}), \mathbf{R}\}, \in \mathbb{R}^{n_{\theta}} \quad (41)$$

418 The matrices $\mathbf{P}, \Lambda, \mathbf{Q}, \mathbf{M}, \mathbf{R}$ are constants, and account for the effects of coarse-graining on
419 the stiffness, output, and forcing matrices. The matrices $\mathbf{D}(\bar{\mathbf{u}}), \mathbf{E}(\bar{\mathbf{u}}), \mathbf{G}(\bar{\mathbf{u}})$ are temperature-
420 dependent matrices, and account for the effects of coarse-graining on the advection matrix
421 due to mesh motion. Leveraging the DG-FEM formula for the advection matrix in Eq. (56c)
422 in the Appendix, and noting that the ablating velocity in Eq. (4) imposes the boundary
423 condition for the mesh motion, the state-dependent matrices for the i -th component are
424 written as,

$$\mathbf{D}(\bar{\mathbf{u}}) \approx \text{diag}[\dot{\mathbf{w}}] \mathbf{D}, \quad \mathbf{G}(\bar{\mathbf{u}}) \approx \mathbf{G} \text{diag}[\dot{\mathbf{w}}], \quad \mathbf{E}(\bar{\mathbf{u}}) \approx \text{diag} \left[\underbrace{\dot{\mathbf{w}}, \dots, \dot{\mathbf{w}}}_{\tilde{m} \text{ times}} \right] \mathbf{E} \quad (42)$$

425 where $\dot{\mathbf{w}} = \dot{\mathbf{w}}(\bar{\mathbf{u}})$ is the SRM based on the observable temperature $\bar{\mathbf{u}}$ and \tilde{m} is the number
426 of hidden states per component so that $m = N\tilde{m}$.

427 The PIROM in Eq. (39) incorporates explicit information on the material properties,
428 boundary conditions, and surface recession, and is designed to generalize across parametric
429 variations in these inputs. Moreover, the hidden dynamics in Eq. (35) are interpretable, as
430 these retain the functional form of the DG-FEM in Eq. (7). The next step is focused on
431 identifying the unknown data-driven parameters Θ characterizing the hidden dynamics.

432 3.3 Learning the Hidden Dynamics

- 433 Learning of the PIROM is achieved through a gradient-based neural-ODE-like approach [3].
 434 For ease of presentation, consider the compact form of the PIROM in Eq. (39),

$$\mathcal{D}(\dot{\mathbf{y}}, \mathbf{y}, \boldsymbol{\xi}, \mathcal{F}; \boldsymbol{\Theta}) = \mathbf{0} \quad (43)$$

435 where $\boldsymbol{\xi}$ defines the model parameters, i.e., SRM parameters, while \mathcal{F} represents the forcing
 436 terms, i.e., the boundary conditions.

437 Consider a dataset of N_s high-fidelity *surface temperature* observable trajectories \mathbf{z}_{HF} ,
 438 sampled at p time instances $\{t_k\}_{k=0}^{p-1}$, for different parameter settings $\{\boldsymbol{\xi}^{(l)}\}_{l=1}^{N_s}$ and forcing
 439 functions $\{\mathcal{F}^{(l)}(t)\}_{l=1}^{N_s}$. The dataset is expressed as,

$$\mathcal{D} = \left\{ \left(t_k, \mathbf{z}_{\text{HF}}^{(l)}(t_k), \boldsymbol{\xi}^{(l)}, \mathcal{F}^{(l)}(t_k) \right) \right\}_{l=1}^{N_s}, \quad k = 0, 1, \dots, p-1 \quad (44)$$

440 In this work, the dataset contains only surface temperature observables – all high-fidelity
 441 information regarding the surface displacements *are assumed to be unavailable during learning*.

443 The learning problem is formulated as the following differentially-constrained problem,

$$\min_{\boldsymbol{\Theta}} \quad \mathcal{J}(\boldsymbol{\Theta}; \mathcal{D}) = \sum_{l=1}^{N_s} \int_{t_0}^{t_f} \ell \left(\mathbf{z}_u^{(l)}, \mathbf{z}_{\text{HF}}^{(l)} \right) dt \quad (45a)$$

$$\text{s.t.} \quad \mathbf{0} = \mathcal{D} \left(\dot{\mathbf{y}}^{(l)}, \mathbf{y}^{(l)}, \boldsymbol{\xi}^{(l)}, \mathcal{F}^{(l)}; \boldsymbol{\Theta} \right) \quad (45b)$$

444 for $l = 1, 2, \dots, N_s$, the objective is to minimize the discrepancy between the high-fidelity
 445 and PIROM predictions for the l -th trajectory with $\ell \left(\mathbf{z}_u^{(l)}, \mathbf{z}_{\text{HF}}^{(l)} \right) = \left\| \mathbf{z}_u^{(l)} - \mathbf{z}_{\text{HF}}^{(l)} \right\|_2^2$.

446 The gradient-based optimization loop is based on the adjoint variable $\boldsymbol{\lambda}$, governed by the
 447 adjoint differential equation,

$$\frac{\partial \ell}{\partial \mathbf{y}} + \boldsymbol{\lambda}^\top \frac{\partial \mathcal{D}}{\partial \mathbf{y}} - \frac{d}{dt} \left(\boldsymbol{\lambda}^\top \frac{\partial \mathcal{D}}{\partial \dot{\mathbf{y}}} \right) = \mathbf{0} \quad (46a)$$

$$\boldsymbol{\lambda}(t_f)^\top \frac{\partial \mathcal{D}}{\partial \dot{\mathbf{y}}(t_f)} = \mathbf{0} \quad (46b)$$

448 Once $\boldsymbol{\lambda}$ is solved, the gradient is computed as,

$$\nabla_{\boldsymbol{\Theta}} \mathcal{J} = \frac{1}{N_s} \sum_{l=1}^{N_s} \int_{t_0}^{t_f} \left(\frac{\partial \ell}{\partial \boldsymbol{\Theta}} + (\boldsymbol{\lambda}^{(l)})^\top \frac{\partial \mathcal{D}}{\partial \boldsymbol{\Theta}} \right) dt \quad (47)$$

449 The PIROM parameters $\boldsymbol{\Theta}$ are updated via stochastic gradient descent using ML optimizers
 450 such as Adam. The learning procedure iterates between solving the PIROM in Eq. (43)
 451 forward in time, solving the adjoint equation in Eq. (46) backward in time, and updating
 452 the parameters $\boldsymbol{\Theta}$ until convergence.

Component	w (cm)	h (cm)	ρ (kg/m ³)	c_p (J/kg·K)	k (W/m·K)	$\alpha \times 10^{-6}$ (m/s·K)
#1	0.3	0.03	160	1200	0.2	1
#2	0.3	0.03	1800	900	5	1
#3	0.3	0.03	300	1500	0.15	1
#4	0.9	0.03	1600	800	10	0

Table 1: Description of TPS components, including thickness h , density ρ , specific heat capacity c_p , thermal conductivity k , and SRM parameter α .

4 Application to Thermal Protection Systems

In this section, the proposed PIROM approach is applied to the analysis of thermo-ablative multi-layered hypersonic TPS. The performance of the PIROM is evaluated in terms of the three corners of the ITM in Fig. 1, based on parametric variations of boundary conditions and SRMs. The results show PIROM to be a promising candidate for the solution of the impossible trinity of modeling, achieving RPM-level computational efficiency and generalizability, while attaining high-fidelity model accuracy.

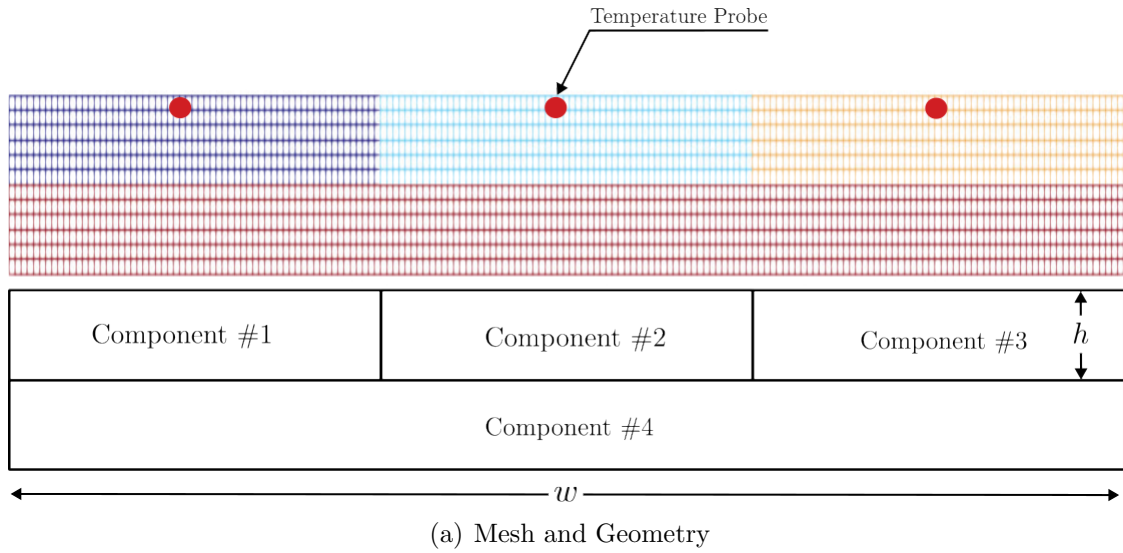
4.1 Problem Definition

Consider the two-dimensional TPS configuration shown in Fig. 3 with constant material properties within each layer, dimensions, and BCs listed in Table 1. Such configuration is representative of the TPS used for the initial concept 3.X vehicle in past studies [10], and involves two main layers: an outer ablative layer, and an inner substrate layer. The top ablative layer may be composed of different materials, such as PICA or Avcoat, while the substrate layer is typically made of a high-temperature resistant material, such as carbon-carbon composite [7]. The ablative layer, composed of $\tilde{N} = 3$ ablative components, is subjected to strong time-varying and non-uniform heating, while the substrate layer, composed of one non-ablative component, is insulated adiabatically at the outer surface; the total number of components is thus $N = 4$.

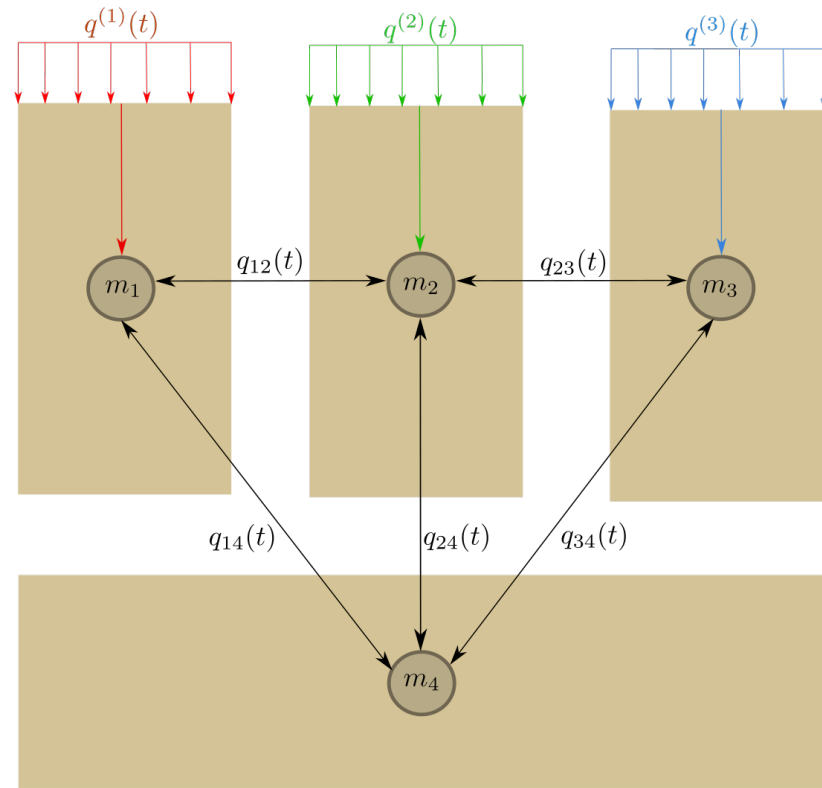
The lumped-mass representation of the TPS configuration is shown in Fig. 3(b), where each component Ω_i is represented by a lumped mass with uniform temperature $\bar{u}_i(t)$. Details regarding the derivation of the LCM for this configuration are provided in Appendix A. The sources of non-linearities studied in this problem originate from the coupling between the thermodynamics and temperature-dependent mesh motion, i.e., geometry-dependent matrices and temperature advection, as well as the heterogeneities across material layers. As shown in Fig. 3, perfect thermocouple devices are placed at the surfaces of the ablative layers for the collection of the high-fidelity temperature signals that are used in the following sections for training and testing the PIROM.

4.2 Problem Parametrization

The operating conditions of the TPS are specified by the boundary conditions, i.e., the heat flux, and the SRM matrix Ξ . Specifically, the heat flux on the Neumann BC is parametrized using $\xi_{BC} = \{\xi_1, \xi_2, \xi_3\}$, while the SRM is parametrized using $\xi_{SRM} = \{\alpha_1, \alpha_2, \alpha_3\}$. Thus,



(a) Mesh and Geometry



(b) Lumped Mass Representation

Figure 3: Four-component TPS geometry and lumped-mass representation for the TPS.

484 the heat flux and SRM over the i -th ablative component are expressed as,

$$q_i(x, t; \boldsymbol{\xi}_{\text{BC}}) = \xi_1 e^{\xi_2 x} e^{\xi_3 t}, \forall x \in \Gamma_{i,q}, \quad \dot{w}_i(z_{u,i}; \boldsymbol{\xi}_{\text{SRM}}) = \alpha_i (z_{u,i} - u_{0,i}), \quad i = 1, \dots, \tilde{N} \quad (48)$$

485 where $\Gamma_{i,q}$, $z_{u,i}$, and $u_{0,i}$ correspond to the Neumann BC surface, the surface temperature
486 prediction, and the initial temperature of the i -th ablative component, respectively. The
487 parameters ξ_1 , ξ_2 , and ξ_3 control the heat flux magnitude, spatial variation, and temporal
488 variation, respectively. The constant α_i is a small material-dependent constant determined
489 from the B' table [12], specifying the surface recession velocity for a given temperature.

490 4.3 Data Generation

491 Full-order solutions of the TPS are computed using the FEM multi-mechanics module from
492 the **Aria** package with the mesh shown in Fig. 3(a) [4]. The mesh consists of 2196 total
493 elements, with 366 elements for each ablative component and 1098 elements for the sub-
494 strate component. Given an operating condition $\boldsymbol{\xi} = [\boldsymbol{\xi}_{\text{BC}}, \boldsymbol{\xi}_{\text{SRM}}]^{\top}$, a high-fidelity solution
495 is computed for one minute, starting from an uniform initial temperature of $T(x, t_0) = 300$
496 K. Each solution consist of a collection of space-time-varying temperature and displacement
497 fields $\left\{ \left(t_k, \mathbf{u}_{\text{HF}}^{(l)}(t_k), \mathbf{d}_{\text{HF}}^{(l)}(t_k), \boldsymbol{\xi}^{(l)} \right) \right\}_{k=0}^{p-1}$, where p is the number of time steps with a step size of
498 $\Delta t \approx 10^{-3}$. The observable trajectories are representative of near-wall thermocouple sensing
499 of hypersonic flows involving heat transfer. At each time instance t_k , a temperature reading
500 is recorded from each ablative component using the thermocouples shown in Fig. 3, resulting
501 in three temperature signals, i.e., the observables $\mathbf{z}_{\text{HF}} \in \mathbb{R}^3$. Therefore, each full-order solu-
502 tion produces one trajectory of observables $\left\{ \left(t_k, \mathbf{z}_{\text{HF}}^{(l)}(t_k), \boldsymbol{\xi}^{(l)} \right) \right\}_{k=0}^{p-1}$. The goal of the PIROM
503 is to predict the surface temperature and displacement as accurately as possible.

504 4.3.1 Definition of Training and Testing Datasets

505 The range of parameters used to generate the training \mathcal{D}_1 and testing $\{\mathcal{D}_2, \mathcal{D}_3\}$ datasets
506 are listed in Table 2. The training and testing datasets are designed, respectively, to: (1)
507 minimize the information that the PIROM can “see”, and (2) to maximize the variabil-
508 ity of test operating conditions to examine the PIROM’s generalization performance. A
509 total of 110 normally-distributed data points for the BC parametrization are visualized in
510 Fig. 4(a), and the corresponding observable trajectories are shown in Figs. 4(b) and 4(c).
511 The training dataset \mathcal{D}_1 includes 10 trajectories with randomly selected BC parameters from
512 the 110 points, with nominal SRM parameters $\boldsymbol{\xi}_{\text{SRM}} = \{1, 1, 1\} \times 10^{-6}$. Note that although
513 Fig. 4(c) shows the surface displacements for all ablative components in \mathcal{D}_1 , only the *surface
514 temperature is used for training the PIROM*.

515 Two additional datasets are generated for testing. The dataset \mathcal{D}_2 includes the remaining
516 100 BC parameter values not considered in \mathcal{D}_1 , and the high-fidelity simulation are generated
517 with the same nominal SRM parameters. The cases in the \mathcal{D}_3 fixes the boundary condition
518 as shown in Fig. 4(a) and varies the SRM parameters as shown in Table. 2. The testing
519 datasets \mathcal{D}_2 and \mathcal{D}_3 are *out-of-distribution* (OOD) datasets, and are meant for testing the
520 generalizability of the ROMs to unseen BCs and SRMs, respectively.

Dataset	Parameters					
	$\xi_1 \times 10^3$	$\xi_2 \times 10^{-1}$	$\xi_3 \times 10^{-2}$	$\alpha_1 \times 10^{-6}$	$\alpha_2 \times 10^{-6}$	$\alpha_3 \times 10^{-6}$
\mathcal{D}_1	[-6.059, -5.902]	[-3.501, 3.152]	[9.670, 10.464]	1	1	1
\mathcal{D}_2	[-6.122, -5.887]	[-3.601, -3.074]	[9.218, 11.246]	1	1	1
\mathcal{D}_3	6	-3.333	10	[0.6, 1.5]	[0.6, 1.5]	[0.6, 1.5]

Table 2: Range of parameters [min, max] in training and testing datasets.

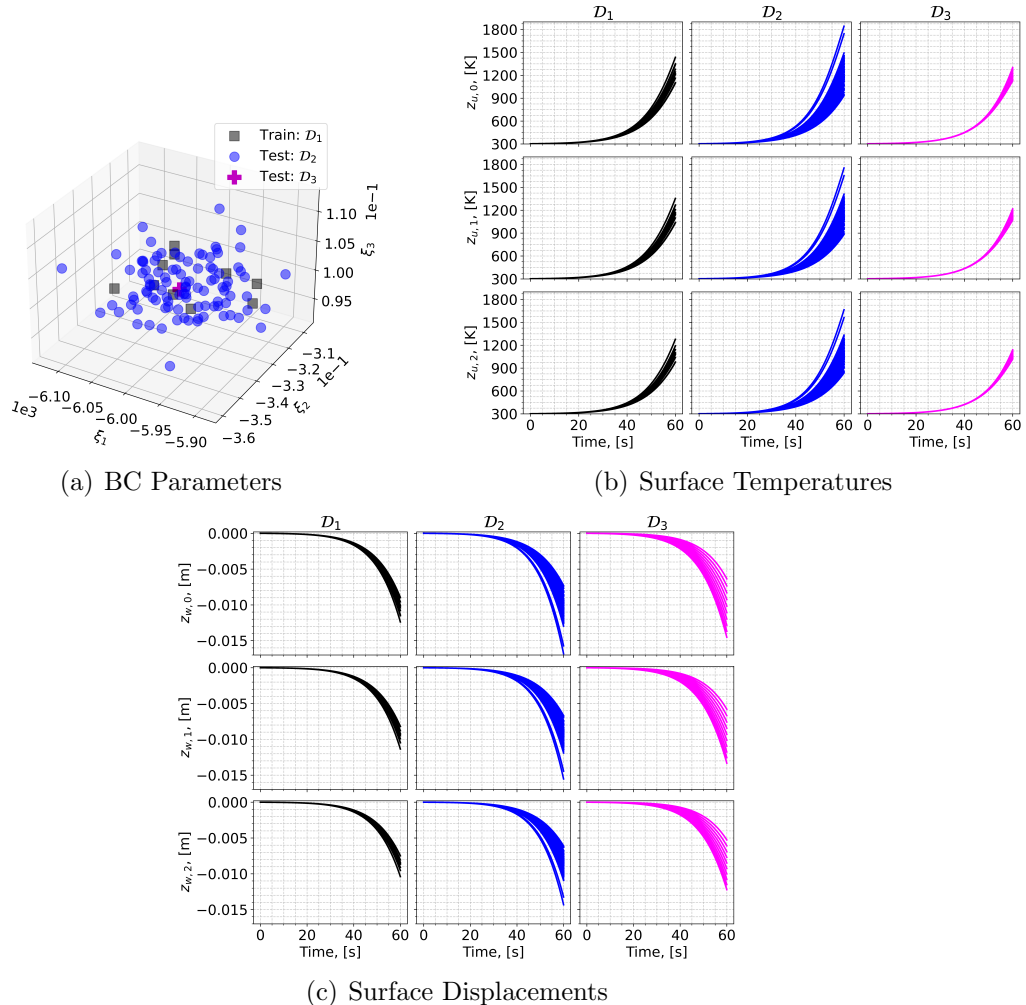


Figure 4: Boundary condition parameters, temperature observables, and displacement observables for the training and testing datasets. The variables $z_{u,i}$ and $z_{w,i}$ correspond to the surface temperature and displacement of the i -th ablative component, respectively.

521 4.4 Performance Metrics

522 The performance metrics are defined to quantitatively assess the solution to the ITM for the
 523 TPS problem. Specifically, the *accuracy* metric quantifies the prediction error of the ROMs
 524 against high-fidelity solutions. The *efficiency* metric quantifies the computational speedup
 525 achieved by the ROMs compared to high-fidelity simulations. The *generalizability* metric
 526 quantifies the ability of the ROMs to retain accuracy when evaluated on OOD datasets.
 527 Together, these metrics provide a comprehensive evaluation of the PIROM's performance
 528 in addressing the challenges associated with modeling complex multi-physics systems. Since
 529 the generalizability metric is inherently tied to the accuracy metric when evaluated on OOD
 530 datasets, the following sections focus on defining the accuracy and efficiency metrics.

531 **Accuracy Metric** Consider one trajectory of high-fidelity surface temperature and dis-
 532 placement data $\left\{ \left(t_k, \mathbf{z}_{u,\text{HF}}^{(l)}(t_k), \mathbf{z}_{w,\text{HF}}^{(l)}(t_k) \right) \right\}_{k=0}^{p-1}$ for the l -th operating condition in the testing
 533 datasets \mathcal{D}_2 or \mathcal{D}_3 . The difference $e_i^{(l)}$ for the i -th predicted observable, denoted as $z_i^{(l)}$, is
 534 computed as,

$$e_i^{(l)} = \frac{1}{\Delta z_i^{(l)}} \sqrt{\frac{1}{p} \sum_{k=0}^{p-1} \left(z_{i,\text{HF}}^{(l)}(t_k) - z_i^{(l)}(t_k) \right)^2} \quad (49)$$

535 for $i = 1, 2, 3$ and $z_i^{(l)} \in \{z_{i,u}^{(l)}, z_{i,w}^{(l)}\}$, and where,

$$\Delta z_i^{(l)} = \max_{0 \leq k \leq p-1} z_{i,\text{HF}}^{(l)}(t_k) - \min_{0 \leq k \leq p-1} z_{i,\text{HF}}^{(l)}(t_k) \quad (50)$$

536 Subsequently, the prediction error of one trajectory is computed by a weighted sum based
 537 on the area of each *ablative component*, resulting in the normalized root mean square error
 538 (NRMSE) metric for one trajectory,

$$\text{NRMSE} = \frac{\sum_{i=1}^{\tilde{N}} |\Omega_i| e_i^{(l)}}{\sum_{i=1}^{\tilde{N}} |\Omega_i|} \times 100\% \quad (51)$$

539 For one dataset, the NRMSE is defined to be the average of the NRMSEs of all trajectories
 540 in the dataset.

541 **Efficiency Metric** The efficiency metric is quantified using the *computational acceleration*,
 542 which focuses on the quantification of the spedup factor $\frac{\mathcal{T}_{\text{HF}}(\mathcal{D})}{\mathcal{T}_{\mathcal{M}}(\mathcal{D})}$. The terms $\mathcal{T}_{\text{HF}}(\mathcal{D})$ and
 543 $\mathcal{T}_{\mathcal{M}}(\mathcal{D})$ correspond to the wall-clock time required by the high-fidelity model and the ROM,
 544 to evaluate all trajectories in the dataset \mathcal{D} , respectively. Here, \mathcal{M} corresponds to the ROM
 545 under consideration, i.e., either the PIROM or the RPM. For a benchmark analysis of the
 546 computational costs during the training phase, please refer to Ref. [18].

547 **4.5 Generalization to Boundary Conditions**

548 To assess generalization to BC, the PIROM and RPM are evaluated on the \mathcal{D}_2 dataset.
549 Temperature trajectory predictions for a representative test case are shown in Figs. 5(a)
550 and 5(b), where the PIROM accurately captures the surface temperature and displacement
551 dynamics, while the RPM exhibits larger deviations and under-predicts surface displace-
552 ments due to the averaging effects of the LCM. The mean NRMSE across all test cases in
553 \mathcal{D}_2 is shown in Figs. 5(e) and 5(f), where the PIROM consistently achieves errors of 1% for
554 both temperature and displacement predictions, improving the RPM's accuracy by an order
555 of magnitude. Figure 5 reports the average substrate temperature, where the LCM remains
556 highly accurate due to the symmetric TPS geometry, adiabatic BCs, and negligible thermal
557 gradients within the substrate. Although the PIROM is trained only on the surface temper-
558 atures of the three ablative components, its hidden dynamics retain the LCM's accuracy for
559 this untrained observable, demonstrating the PIROM's ability to generalize and preserve the
560 underlying physics of the reduced-physics backbone. The consistent low predictions errors
561 demonstrate the solution to the *accuracy* corner of the ITM.

562 **4.6 Generalization to Surface Recession Models**

563 The generalization performance of the PIROM and RPM is also evaluated on surface reces-
564 sion models using the OOD \mathcal{D}_3 dataset. As detailed in Table 1, the SRM parameter α in \mathcal{D}_3
565 is perturbed 10 times by up to $\pm 50\%$ from their nominal values. The SRM model perturba-
566 tion introduces significant changes to the ablative layer dynamics, potentially increasing the
567 rate of ablation at lower temperatures, as shown in Figs. 5(c) and 5(d). The PIROM, with-
568 out considering any SRM variations during training, is able to accurately predict the surface
569 temperature and displacement dynamics for the perturbed SRMs. Figures 5(e) and 5(f) show
570 the mean NRMSE across all test cases in \mathcal{D}_3 , where the PIROM consistently achieves errors
571 below 1% for both temperature and displacement predictions, and consistently improves the
572 RPM's accuracy by approximately an order of magnitude. The consistent low prediction
573 errors demonstrate the solution to the *generalizability* corner of the ITM.

574 **4.7 Computational Cost**

575 All computations are performed in serial for fairness on an Intel Xeon (R) Gold 6258R
576 CPU 2.70GHz computer with 62 GB of RAM. The numerical integration for the RPM
577 and PIROM models are performed using SciPy's `solve_ivp` function with default settings.
578 Provided a parametrization for the BC and SRM, the high-fidelity FEM simulation takes
579 about ≈ 60 seconds, the RPM takes about ≈ 0.137 seconds, and the PIROM takes about
580 ≈ 0.280 seconds. Therefore, during evaluation both the RPM and PIROM achieve speedup
581 factors of approximately 438 and 214, respectively, over the high-fidelity model. As a result,
582 the PIROM and RPM are *two-orders-of-magnitude faster* than the high-fidelity model. The
583 PIROM nearly preserves the computational efficiency of the RPM (about twice as expensive
584 as the RPM), while achieving significantly higher accuracy and generalization capabilities.
585 The results demonstrate the benefits of physics-infused modeling for the development of
586 efficient and generalizable ROMs for complex multi-physics systems, and demonstrate the

587 solution to the *efficiency* corner of the ITM.

588 4.8 Summary of Results

589 The results presented in this section demonstrate the accuracy, generalizability, and com-
590 putational efficiency of the proposed PIROM approach for the analysis of thermo-ablative
591 multi-layered hypersonic TPS. The PIROM consistently achieves low prediction errors below
592 1% for both surface temperature and displacement across a range of unseen boundary con-
593 ditions and surface recession models. Furthermore, the PIROM retains the computational
594 efficiency of traditional RPMs, achieving speedup factors of over 200 times compared to high-
595 fidelity FEM simulations. The generalization capabilities of the PIROM are attributed to its
596 hybrid structure: a physics-based LCM backbone that ensures consistency with the under-
597 lying thermodynamics, while a data-driven correction mechanism captures the un-resolved
598 dynamics. For this TPS problem, the PIROM successfully addresses the impossible trinity of
599 modeling, achieving high-fidelity model accuracy, RPM-level computational efficiency, and
600 generalizability to unseen operating conditions.

601 5 Conclusions

602 This work presents the development and validation of the *scientific machine learning* frame-
603 work termed *Physics-Informed Reduced Order Model* (PIROM) for simulating the transient
604 thermo-ablative response of hypersonic thermal protection systems (TPS) subjected to hy-
605 personic boundary layers. Using coarse-graining on a DG-FEM model and the Mori-Zwanzig
606 formalism, the PIROM formulation in Ref. [18] is extended to account for non-decomposing
607 thermo-ablative response of a multi-layered TPS. The PIROM builds upon the following two
608 key components: (1) a first-order physics-based model, i.e., the RPM based on LCM and
609 SRM, for low-fidelity predictions of the surface temperature and recession; and (2) a data-
610 driven closure to the non-Markovian term in the Generalized Langevin Equation (GLE). The
611 non-Markovian closure is recast as a set of hidden states that evolve according to a data-
612 driven dynamical system that is learned from a sparse collection of high-fidelity temperature
613 signals.

614 The results demonstrate that the PIROM framework effectively reconciles the trade-offs
615 between accuracy, generalizability, and efficiency of the ITM for simulating ablating hy-
616 personic TPS. The PIROM consistently achieves mean observable prediction errors of less
617 than 1% for extrapolative settings involving time-and-space varying boundary conditions
618 and SRM models. Notably, the PIROM improves the RPM’s accuracy by an order of magni-
619 tude while preserving its computational efficiency, physical interpretability, and parametric
620 generalizability. Moreover, the PIROM delivers online evaluations that are two orders of
621 magnitude faster than the FOM. These results highlight the PIROM’s potential as a promis-
622 ing framework for optimizing multi-physical dynamical systems, such as TPS under diverse
623 operating conditions.

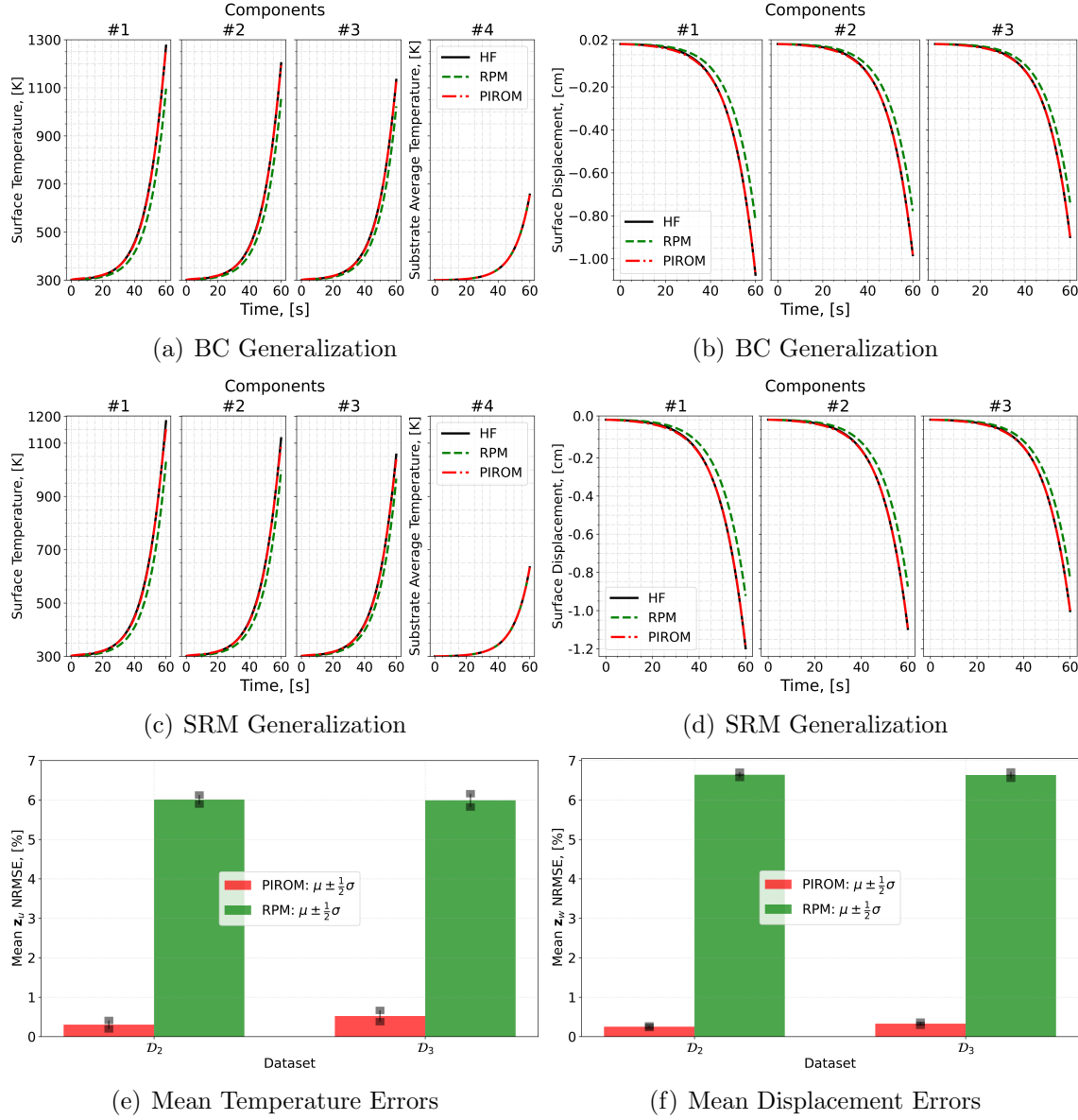


Figure 5: PIROM predictions against high-fidelity solutions for (a)-(b) BC generalization, (c)-(d) SRM generalization, and (e)-(f) mean errors across testing datasets.

624 **Acknowledgments**

625 Sandia National Laboratories is a multimission laboratory managed and operated by Na-
626 tional Technology & Engineering Solutions of Sandia, LLC, a wholly owned subsidiary of
627 Honeywell International Inc., for the U.S. Department of Energy's National Nuclear Secu-
628 rity Administration under contract DE-NA0003525. This paper describes objective technical
629 results and analysis. Any subjective views or opinions that might be expressed in the pa-
630 per do not necessarily represent the views of the U.S. Department of Energy or the United
631 States Government. This article has been co-authored by an employee of National Tech-
632 nology & Engineering Solutions of Sandia, LLC under Contract No. DE-NA0003525 with
633 the U.S. Department of Energy (DOE). The employee owns all right, title and interest
634 in and to the article and is solely responsible for its contents. The United States Gov-
635 ernment retains and the publisher, by accepting the article for publication, acknowledges
636 that the United States Government retains a non-exclusive, paid-up, irrevocable, world-
637 wide license to publish or reproduce the published form of this article or allow others to
638 do so, for United States Government purposes. The DOE will provide public access to
639 these results of federally sponsored research in accordance with the DOE Public Access Plan
640 <https://www.energy.gov/downloads/doe-public-access-plan>.

641 A Technical Details

642 This appendix presents the technical details of the PIROM framework applied to the trans-
643ient modeling of thermo-ablative TPS. The first section provides the mathematical details
644 for the definition of the DG-FEM. The second section details the coarse-graining proce-
645 dures performed on the DG-FEM representation of the TPS. The third section presents the
646 derivation of the LCM model from an energy-conservation perspective.

647 A.1 Full-Order Model

648 To obtain the full-order numerical solution, the governing equation is spatially discretized
649 using variational principles of Discontinuous Galerkin (DG) to result in a high-dimensional
650 system of ordinary differential equations (ODEs). The DG-FEM model is written in an
651 element-wise form, which is beneficial for subsequent derivations of the lower-order models.
652 Note that the choice of DG approach here is mainly for theoretical convenience in the sub-
653 sequent coarse-graining formulation. In the numerical results, the full-order TPS ablation
654 simulations is computed using standard FEM instead, and the equivalence between DG and
655 standard FEM is noted upon their convergence.

656 A.1.1 Domain Discretization

657 Consider a conforming mesh partition of the domain in Fig. 3, where each element belongs
658 to one and only one component. Denote the collection of all M elements as $\{E_i\}_{i=1}^M$. To ease
659 the description of the DG model, a graph structure is employed. The elements are treated
660 as vertices, the set of which is denoted $\mathcal{V} = \{m\}_{m=1}^M$. Two neighboring elements, E_i and E_j ,
661 are connected by an edge (i, j) , and the shared boundary between them is denoted e_{ij} . The
662 collection of all edges are denoted \mathcal{E} , and \mathcal{G} is referred to as a graph. In the graph, the edges
663 are unidirected, meaning if $(i, j) \in \mathcal{E}$ then $(j, i) \in \mathcal{E}$. Furthermore, denote the neighbors
664 of the i -th element as $\mathcal{N}_i = \{j | (i, j) \in \mathcal{E}\}$. Lastly, for the ease of notation, introduce two
665 special indices: T for the boundary of an element that overlaps with the Dirichlet boundary
666 condition, and similarly q for the Neumann boundary condition.

667 A.1.2 Weak Form of Discontinuous Galerkin Method

668 Choosing appropriate basis functions ϕ_k and ϕ_l and using the Interior Penalty Galerkin
669 (IPG) scheme [5], the variational bilinear form for Eq. (1a) is,

$$\sum_{i=1}^M a_{\epsilon,i}(\phi_k, \phi_l) = \sum_{i=1}^M L_i(\phi_k) \quad (52)$$

670 where ϵ is an user-specified parameter and,

$$a_{\epsilon,i}(\phi_k, \phi_l) = \int_{E_i} \left(\rho c_p \phi_k \frac{\partial \phi_l}{\partial t} + \mathbf{k} \nabla \phi_k \cdot \nabla \phi_l - \rho c_p \phi_k \mathbf{v} \cdot \nabla \phi_l \right) dE_i \quad (53a)$$

$$\begin{aligned} & - \sum_{j \in \mathcal{N}_i \cup \{T_b\}} \int_{e_{ij}} \{ \mathbf{k} \nabla \phi_k \cdot n \} [\phi_l] de_{ij} + \epsilon \sum_{j \in \mathcal{N}_i \cup \{T_b\}} \int_{e_{ij}} \{ \mathbf{k} \nabla \phi_l \cdot n \} [\phi_k] de_{ij} \\ & + \sigma \sum_{j \in \mathcal{N}_i \cup \{T_b\}} \int_{e_{ij}} [\phi_k] [\phi_l] de_{ij} \end{aligned} \quad (53b)$$

$$L_i(v) = \epsilon \sum_{j \in \mathcal{N}_i \cup \{T_b\}} \int_{e_{ij}} (\mathbf{k} \nabla \phi_l \cdot n) T_b de_{ij} + \int_{e_{iq}} \phi_k q_b de_{iq} + \sigma \int_{e_{iT}} \phi_k T_b de_{iT} \quad (53c)$$

671 In the bi-linear form above, the notations $[]$ and $\{ \}$ are respectively the jumps and averages
672 at the boundary e_{ij} share by two elements E_i and E_j ,

$$[u] = u|_{E_i} - u|_{E_j}, \quad \{u\} = \frac{1}{2} \left(u|_{E_i} + u|_{E_j} \right), \quad \text{for } x \in e_{ij} = E_i \cap E_j$$

673 Moreover, the terms associated with σ are introduced to enforce the Dirichlet boundary
674 conditions; σ is a penalty factor whose value can depend on the size of an element. Depending
675 on the choice of ϵ , the bi-linear form corresponds to symmetric IPG ($\epsilon = -1$), non-symmetric
676 IPG ($\epsilon = 1$), and incomplete IPG ($\epsilon = 0$). All these schemes are consistent with the
677 original PDE and have similar convergence rate with respect to mesh size. In the following
678 derivations, the case $\epsilon = 0$ is chosen for the sake of simplicity.

679 A.1.3 Discontinuous Galerkin Model

680 Next, the DG-based model is written in an element-wise form. For the i -th element, use a
681 set of P trial functions to represent the temperature as in Eq. (6). Without loss of generality,
682 the trial functions are assumed to be orthogonal, so that,

$$\int_{E_i} \phi_l^i(x) \phi_k^i(x) d\Omega = 0, \quad l \neq k$$

683 where $|E_i|$ is the area ($n_d = 2$) or volume ($n_d = 3$) of the i -th element, and δ_{lk} is the Kronecker
684 delta function. Furthermore, for simplicity, choose $\phi_1^i = 1$. Thus, by orthogonality,

$$\int_{E_i} \phi_1^i(x) d\Omega = |E_i|, \quad \int_{E_i} \phi_k^i(x) d\Omega = 0, \quad k = 2, 3, \dots, P$$

685 Under the choice of basis functions, u_1^i is simply the average temperature of element E_i ,
686 denoted as \bar{u}_i .

687 Using test functions same as trial functions, the dynamics \mathbf{u}_i is obtained by evaluating
688 the element-wise bi-linear forms,

$$a_{\epsilon,i}(\phi_k^i, T^i) = L_i(\phi_k^i), \quad k = 1, 2, \dots, P \quad (54)$$

689 Therefore, by standard variational principles, e.g., [5], the element-wise governing equation
690 is denoted as,

$$\mathbf{A}^i \dot{\mathbf{u}}_i = (\mathbf{B}^i + \mathbf{C}^i) \mathbf{u}_i + \sum_{j \in \mathcal{N}_i \cup \{T_b\}} (\mathbf{B}_{ij}^i \mathbf{u}_i + \mathbf{B}_{ij}^j \mathbf{u}_j) + \mathbf{f}_i(t), \quad \text{for } i = 1, 2, \dots, M \quad (55)$$

691 where for $k, l = 1, 2, \dots, P$,

$$[\mathbf{A}^i]_{kl} = \int_{E_i} \rho c_p \phi_k^i \phi_l^i dE_i \quad (56a)$$

$$[\mathbf{B}^i]_{kl} = - \int_{E_i} (\nabla \phi_k^i) \cdot (\mathbf{k} \nabla \phi_l^i) dE_i \quad (56b)$$

$$[\mathbf{C}^i]_{kl} = \int_{E_i} \rho c_p \phi_k^i \mathbf{v}_m^i \cdot \nabla \phi_l^i dE_i \quad (56c)$$

$$[\mathbf{B}_{ij}^i] = \int_{e_{ij}} \{ \mathbf{k} \nabla \phi_k^i \cdot \hat{n} \} \phi_l^i - \sigma [\phi_k^i] \phi_l^i de_{ij} \quad (56d)$$

$$[\mathbf{B}_{ij}^j] = \int_{e_{ij}} - \{ \mathbf{k} \nabla \phi_k^i \cdot \hat{n} \} \phi_l^j + \sigma [\phi_k^i] \phi_l^j de_{ij} \quad (56e)$$

$$[\mathbf{f}^i]_k = \int_{e_{iq}} \phi_k^i q_b de_{iq} + \sigma \int_{e_{iT}} \phi_k^i de_{iT} \quad (56f)$$

692 The matrices $\mathbf{A}^i \in \mathbb{R}^{P \times P}$, $\mathbf{B}^i \in \mathbb{R}^{P \times P}$, and $\mathbf{C}^i \in \mathbb{R}^{P \times P}$ are respectively the capacitance,
693 conductivity, and advection matrices for element i . These matrices depend on ρ , c_p , \mathbf{k} , and
694 \mathbf{v} , and hence can be non-linear functions of \mathbf{u}_i . Since the trial functions are orthogonal, if
695 ρc_p is constant within an element, \mathbf{A}^i is diagonal; otherwise, \mathbf{A}^i is symmetric and positive
696 definite as $\rho c_p > 0$.

697 For compactness, the element-wise model in Eq. (55) is also written in matrix form,

$$\mathbf{A} \dot{\mathbf{u}} = [\mathbf{B} + \mathbf{C}(\mathbf{u})] \mathbf{u} + \mathbf{f}(t) \quad (57)$$

698 where $\mathbf{u} = [\mathbf{u}^{(1)}, \mathbf{u}^{(2)}, \dots, \mathbf{u}^{(M)}]^T \in \mathbb{R}^{MP}$ includes all DG variables, $\mathbf{f} = [\mathbf{f}^{(1)}, \mathbf{f}^{(2)}, \dots, \mathbf{f}^{(M)}]^T \in$
699 \mathbb{R}^{MP} , \mathbf{A} and \mathbf{C} are matrices of M diagonal blocks whose i -th blocks are \mathbf{A}^i and \mathbf{C}^i , and \mathbf{B}
700 is a matrix of $M \times M$ blocks whose (i, j) -th block is,

$$\mathbf{B}_{ij} = \begin{cases} \mathbf{B}^i + \sum_{j \in \mathcal{N}_i \cup \{T_b\}} \mathbf{B}_{ij}^i, & i = j \\ \mathbf{B}_{ij}^j, & i \neq j \end{cases} \quad (58)$$

701 The dependency of \mathbf{C} on \mathbf{u} is explicitly noted in Eq. (57), which is the main source of
702 non-linearity in the current TPS problem. Moreover, the mesh velocity \mathbf{v} varies with space
703 and time, and thus the advection matrix \mathbf{C} varies with time as a function of the surface
704 temperature $T_q(x, t)$.

705 A.2 Coarse-Graining of Dynamics

706 The LCM is obtained by coarse-graining the full-order DG-FEM. This coarse-graining pro-
 707 cedure produces resolved $\mathbf{r}^{(1)}(\bar{\mathbf{u}}, t)$ and residual $\mathbf{r}^{(2)}(\mathbf{u}, t)$ dynamics as in Eq. (24). This
 708 section presents the detail derivations and magnitude analysis for the resolved and residual
 709 dynamics.

710 A.2.1 Resolved Dynamics

711 Using Eq. (21), the resolved dynamics is computed as follows,

$$\mathbf{r}^{(1)}(\bar{\mathbf{u}}, t) = \mathcal{P} [\Phi^+ \mathbf{A}^{-1} (\mathbf{B}\mathbf{u} + \mathbf{C}(\mathbf{u})\mathbf{u} + \mathbf{f}(t))] \quad (59a)$$

$$= \Phi^+ \mathbf{A}^{-1} \mathbf{P} \mathbf{B} \mathbf{P} \mathbf{u} + \Phi^+ \mathbf{A}^{-1} \mathbf{P} \mathbf{C} (\mathbf{P} \mathbf{u}) \mathbf{P} \mathbf{u} + \Phi^+ \mathbf{A}^{-1} \mathbf{P} \mathbf{f}(t) \quad (59b)$$

$$= \underbrace{\Phi^+ \mathbf{A}^{-1} \Phi}_{\#1} \underbrace{\Phi^+ \mathbf{B} \Phi \bar{\mathbf{u}}}_{\#2} + \Phi^+ \mathbf{A}^{-1} \Phi \underbrace{\Phi^+ \mathbf{C} (\Phi \bar{\mathbf{u}}) \Phi}_{\#3} \bar{\mathbf{u}} + \Phi^+ \mathbf{A}^{-1} \Phi \underbrace{\Phi^+ \mathbf{f}(t)}_{\#4} \quad (59c)$$

712 Detailed derivations for the #1, #2, and #4 terms can be found in Ref. [18] for the case
 713 of temperature-varying matrices, where it is shown that coarse-graining the capacitance,
 714 conductivity, and forcing terms result exactly in the LCM matrices. The remaining term #3
 715 is analyzed next.

716 **Term #3** The $\mathbf{C}(\mathbf{u}) \in \mathbb{R}^{MP \times MP}$ matrix contains M diagonal of size $P \times P$, since the
 717 basis functions are defined locally on each element. Therefore, $[\mathbf{C}(\mathbf{u})]_{ij} = \mathbf{0}$ for all $i \neq j$ with
 718 $i, j = 1, 2, \dots, M$. It follows that for $k, l = 1, 2, \dots, N$,

$$[\Phi^+ \mathbf{C}(\Phi \bar{\mathbf{u}}) \Phi]_{kl} = \sum_{i=1}^M \sum_{j=1}^M \varphi_i^{k+} [\mathbf{C}(\Phi \bar{\mathbf{u}})]_{ij} \varphi_j^l \quad (60a)$$

$$= \sum_{i=1}^M \varphi_i^{k+} [\mathbf{C}(\Phi \bar{\mathbf{u}})]_{ii} \varphi_i^l \quad (60b)$$

$$= \sum_{i \in \mathcal{V}_k} \varphi_i^{k+} [\mathbf{C}(\Phi \bar{\mathbf{u}})]_{ii} \varphi_i^l \quad (60c)$$

719 where in the second row, the fact that $[\mathbf{C}(\mathbf{u})]_{ij} = 0$ for all $i \neq j$ is used, and in the last row,
 720 the fact that $\varphi_i^{k+} = 0$ for all $i \notin \mathcal{V}_k$ is used. Now, considering that $[\mathbf{C}(\mathbf{u})]_{ii}$ has a (1, 1)-th
 721 zero element, i.e., $[C_{11}(\Phi \bar{\mathbf{u}})]_{ii} = 0$, and that if $k \neq l$ then $i \notin \mathcal{V}_l$ and thus $\varphi_i^l = \mathbf{0}$, it follows
 722 that for some index $i \in \mathcal{V}_k$,

$$\varphi_i^{k+} [\mathbf{C}(\Phi \bar{\mathbf{u}})]_{ii} \varphi_i^l = \varphi_i^{k+} [\mathbf{C}(\Phi \bar{\mathbf{u}})]_{ii} \varphi_i^k = \frac{|E_i|}{|\Omega_k|} [C_{11}(\Phi \bar{\mathbf{u}})]_{ii} = 0 \quad (61)$$

723 The matrix $[\Phi^+ \mathbf{C}(\Phi \bar{\mathbf{u}}) \Phi]_{kl} = 0$ for all $k, l = 1, 2, \dots, N$, and thus,

$$\bar{\mathbf{C}}(\bar{\mathbf{u}}) = \Phi^+ \mathbf{C}(\Phi \bar{\mathbf{u}}) \Phi = \mathbf{0} \quad (62)$$

⁷²⁴ as indicated by the LCM in Eq. (11).

⁷²⁵ A.2.2 Magnitude Analysis for Residual Dynamics

⁷²⁶ Next, the magnitude of the residual dynamics $\mathbf{r}^{(2)}(\mathbf{u}, t)$ is analyzed to pinpoint the missing
⁷²⁷ physics in the LCM. By definition,

$$\mathbf{r}^{(2)}(\mathbf{u}, t) = \dot{\bar{\mathbf{u}}} - \mathbf{r}^{(1)}(\bar{\mathbf{u}}, t) \quad (63a)$$

$$= \Phi^+ \mathbf{r}(\mathbf{u}, t) - \mathbf{r}^{(1)}(\bar{\mathbf{u}}, t) \quad (63b)$$

$$= \underbrace{\Phi^+ \mathbf{A}^{-1} \mathbf{B} \mathbf{u} - \bar{\mathbf{A}}(\mathbf{w})^{-1} \bar{\mathbf{B}}(\mathbf{w}) \bar{\mathbf{u}}}_{\#1} + \underbrace{\Phi^+ \mathbf{A}^{-1} \mathbf{C}(\mathbf{u}) \mathbf{u} - \bar{\mathbf{A}}(\mathbf{w})^{-1} \bar{\mathbf{C}}(\bar{\mathbf{u}}) \bar{\mathbf{u}}}_{\#2} \quad (63c)$$

$$+ \underbrace{\Phi^+ \mathbf{A}^{-1} \mathbf{f}(t) - \bar{\mathbf{A}}(\mathbf{w})^{-1} \bar{\mathbf{f}}(t)}_{\#3} \quad (63d)$$

⁷²⁸ The magnitude analysis for terms $\#1$ and $\#3$ can be found in Ref. [18] for temperature-
⁷²⁹ varying material properties. The remaining term $\#2$ is analyzed next. Let $\mathbf{D}(\bar{\mathbf{u}}) = \mathbf{A}^{-1} \mathbf{P} \mathbf{C}(\Phi \bar{\mathbf{u}})$
⁷³⁰ so that,

$$\Phi^+ \mathbf{A}^{-1} \mathbf{C}(\mathbf{u}) \mathbf{u} - \bar{\mathbf{A}}(\mathbf{w})^{-1} \bar{\mathbf{C}}(\bar{\mathbf{u}}) \bar{\mathbf{u}} \quad (64a)$$

$$= \Phi^+ \mathbf{A}^{-1} \mathbf{C}(\mathbf{u}) \mathbf{u} - \Phi^+ \mathbf{A}^{-1} \mathbf{P} \mathbf{C}(\Phi \bar{\mathbf{u}}) \Phi \Phi^+ \mathbf{u} \quad (64b)$$

$$= \Phi^+ \mathbf{A}^{-1} \mathbf{C}(\mathbf{u}) \mathbf{u} - \Phi^+ \mathbf{D}(\bar{\mathbf{u}}) \Phi \Phi^+ \mathbf{u} \quad (64c)$$

$$(64d)$$

⁷³¹ where $\mathbf{P} = \Phi \Phi^+$. Thus,

$$\|\Phi^+ \mathbf{A}^{-1} \mathbf{C}(\mathbf{u}) \mathbf{u} - \bar{\mathbf{A}}(\mathbf{w})^{-1} \bar{\mathbf{C}}(\bar{\mathbf{u}}) \bar{\mathbf{u}}\| \quad (65a)$$

$$\leq \|\Phi^+ \mathbf{A}^{-1} \mathbf{C}(\mathbf{u}) \mathbf{u} - \Phi^+ \mathbf{D}(\bar{\mathbf{u}}) \mathbf{u}\| + \|\Phi^+ \mathbf{D}(\bar{\mathbf{u}}) \mathbf{u} - \Phi^+ \mathbf{D}(\bar{\mathbf{u}}) \Phi \Phi^+ \mathbf{u}\| \quad (65b)$$

$$\leq \|\Phi^+\| \underbrace{\|\mathbf{A}^{-1} \mathbf{C}(\mathbf{u}) \mathbf{u} - \mathbf{D}(\bar{\mathbf{u}}) \mathbf{u}\|}_{\#1} + \|\Phi^+ \mathbf{D}(\bar{\mathbf{u}})\| \underbrace{\|\mathbf{u} - \Phi \Phi^+ \mathbf{u}\|}_{\#2} \quad (65c)$$

⁷³² Similar to the analysis in Ref. [18], term $\#2$ is due to the approximation of non-uniform
⁷³³ temperature as constants in each component, and the term $\#1$ is the error in the advection
⁷³⁴ effects due to such approximation.

⁷³⁵ A.3 Lumped Capacitance Model

⁷³⁶ The following assumptions are employed: (1) the temperature in the i -component is described
⁷³⁷ by a scalar time-varying average temperature \bar{u}_i , (2) between neighboring components (i)
⁷³⁸ and (j) the heat flux is approximated as,

$$q_{ij} = \frac{\bar{u}_j - \bar{u}_i}{R_{ij}} \quad (66)$$

739 where R_{ij} is the thermal resistance. Empirically, for a component of isotropic heat conduction
 740 conductivity k , length ℓ , and cross-section area A , the thermal resistance is $R = \ell/kA$. Between
 741 components i and j , define $R_{ij} = R_i + R_j$. In addition, the heat flux due to Dirichlet
 742 boundary condition is computed as $q_{iT} = (T_b - \bar{u}_i)/R_i$.

743 At component i , the dynamics of LCM are given by,

$$\int_{E_i} \rho c_p \dot{\bar{u}}_i dE_i = \left(\sum_{j \in \mathcal{N}_i} \int_{e_{ij}} \frac{\bar{u}_j - \bar{u}_i}{R_{ij}} de_{ij} \right) + \int_{e_{iq}} q_b de_{iq} + \int_{e_{iT}} \frac{T_b - \bar{u}_i}{R_i} de_{iT} \quad (67a)$$

$$\bar{A}_i \dot{\bar{u}}_i = \left(\sum_{j \in \mathcal{N}_i} \frac{|e_{ij}|}{R_{ij}} (\bar{u}_j - \bar{u}_i) \right) + |e_{iq}| \bar{q}_i + \frac{|e_{iT}|}{R_i} (\bar{T}_i - \bar{u}_i) \quad (67b)$$

$$= \sum_{j \in \mathcal{N}_i} \left(-\frac{|e_{ij}|}{R_{ij}} \bar{u}_i + \frac{|e_{ij}|}{R_{ij}} \bar{u}_j \right) + \left(-\frac{|e_{iT}|}{R_i} \bar{u}_i \right) + \left(|e_{iq}| \bar{q}_i + \frac{|e_{iT}|}{R_i} \bar{T}_i \right) \quad (67c)$$

$$= \sum_{j \in \mathcal{N}_i \cup \{T_b\}} (\bar{B}_{ij}^i \bar{u}_i + \bar{B}_{ij}^j \bar{u}_j) + \bar{f}_i \quad (67d)$$

744 where in Eq. (67b) $|e|$ denotes the length ($d = 2$) or area ($d = 3$) of a component boundary
 745 e . The \bar{A}_i , \bar{B}_{ij}^i , and \bar{B}_{ij}^j quantities are provided in Eq. (14).

746 The lumped-mass representation for the four-component TPS is shown in Fig. 3. Let
 747 $\mathbf{w} \in \mathbb{R}^{\tilde{N}}$ be the one-dimensional surface displacements of the ablative TPS components, v_i
 748 represent the area of the i -th component, $\bar{\rho}c_{p,i}$, the constant heat capacitance, and $1/R_{ij} =$
 749 $1/R_i + 1/R_j$ the equivalent thermal resistance between i and j . Note that the areas and
 750 equivalent thermal resistances vary with \mathbf{w} due to ablation. Leveraging the formulas from
 751 Eqs. (13) and (14), the LCM matrices are given by,

$$\bar{\mathbf{A}} = \begin{bmatrix} \bar{\rho}c_{p,1} v_1 & 0 & 0 & 0 \\ 0 & \bar{\rho}c_{p,2} v_2 & 0 & 0 \\ 0 & 0 & \bar{\rho}c_{p,3} v_3 & 0 \\ 0 & 0 & 0 & \bar{\rho}c_{p,4} v_4 \end{bmatrix}, \quad (68a)$$

$$\bar{\mathbf{B}} = \begin{bmatrix} \frac{1}{R_{12}} + \frac{1}{R_{14}} & -\frac{1}{R_{12}} & 0 & -\frac{1}{R_{14}} \\ -\frac{1}{R_{12}} & \frac{1}{R_{12}} + \frac{1}{R_{24}} + \frac{1}{R_{23}} & -\frac{1}{R_{23}} & -\frac{1}{R_{24}} \\ 0 & -\frac{1}{R_{32}} & \frac{1}{R_{32}} + \frac{1}{R_{34}} & -\frac{1}{R_{34}} \\ -\frac{1}{R_{14}} & -\frac{1}{R_{24}} & -\frac{1}{R_{34}} & \frac{1}{R_{14}} + \frac{1}{R_{24}} + \frac{1}{R_{34}} \end{bmatrix}, \quad \bar{\mathbf{f}} = \begin{bmatrix} \bar{q}^{(1)} \\ \bar{q}^{(2)} \\ \bar{q}^{(3)} \\ 0 \end{bmatrix} \quad (68b)$$

752 References

- 753 [1] Adam J. Amar, A. Brandon Oliver, Benjamin S. Kirk, Giovanni Salazar, and Justin
 754 Droba. Overview of the charring ablator response (char) code. In AIAA, editor, *AIAA
 755 Aviation Forum*, 2016.
- 756 [2] Guy L. Bergel, Frank B. Beckwith, Gabel J. de Frias, Kevin M. Manktelow, Mark T.
 757 Merewether, Scott T. Miller, Krishen J. Parmar, Timothy S. Shelton, Jesse T. Thomas,

- 758 Jeremy T. Trageser, Benjamin T. Treweek, Michael V. Veilleux, and Ellen B. Wagman.
 759 *Sierra/SolidMechanics 5.6 User's Manual*, 2022.
- 760 [3] Ricky T. Q. Chen, Yulia Rubanova, Jesse Bettencourt, and David Duvenaud. Neural
 761 ordinary differential equations, 2019.
- 762 [4] Jonathan Clausen, Victor Brunini, Lincoln Collins, Robert C Knaus, Alec Kucala,
 763 Stephen Lin, Daniel Robert Moser, Malachi Phillips, Thomas Michael Ransegrenola,
 764 Samuel Ramirez Subia, et al. Sierra multimechanics module: Aria verification manual-
 765 version 5.22. Technical report, Sandia National Lab.(SNL-NM), Albuquerque, NM
 766 (United States), 2024.
- 767 [5] Gary Cohen and Sebastien Pernet. *Finite Element and Discontinuous Galerkin Methods
 768 for Transient Wave Equations*. Springer Dordrecht, Le Chesnay and Toulouse France,
 769 2018.
- 770 [6] Jianhao Fang, Weifei Hu, Zhenyu Liu, Yuhao Zhou, Chao Wei, and Jianrong Tan. A
 771 reduced order finite element-informed surrogate model for approximating global high-
 772 fidelity simulations. *Structural and Multidisciplinary Optimization*, 67(12), 2024.
- 773 [7] Matthew Gasch, Keith Peterson, Mairead Stackpoole, Ethiraj Venkatapathy, Gregory
 774 Gonzales, and Kyle Hendrickson. Development of advanced ablative carbon phenolic
 775 tps for future nasa missions and commercial space. In *38th Annual Small Satellite
 776 Conference*, Logan, Utah, May 2024.
- 777 [8] Micah A. Howard and Ben F. Blackwell. A multi-dimensional finite element based solver
 778 for decomposing and non-decomposing thermal protection systems. In AIAA, editor,
 779 *AIAA Aviation Forum*, 2015.
- 780 [9] Frank P. Incropera, David P. DeWitt, Theodore L. Bergman, and Adrienne S. Lavine.
 781 *Fundamentals of Heat and Mass Transfer*. Wiley, Hoboken, NJ, 7th edition, 2011.
- 782 [10] R. J. Klock and Carlos Cesnik. Nonlinear thermal reduced-order modeling for hypersonic
 783 vehicles. *AIAA Journal*, 55(7), 2017.
- 784 [11] Arun Govind Neelan. Linear and non-linear reduced order model of scramjet. In *Ad-
 785 vances in Multidisciplinary Design, Analysis and Optimization*, pages 111–118, Singa-
 786 pore, 2025.
- 787 [12] Alberto Padovan, Blaine Vollmer, Francesco Panerai, Marco Panesi, Kelly A. Stephani,
 788 and Daniel J. Bodony. An extended bformulation for ablating-surface boundary condi-
 789 tions. *International Journal of Heat and Mass Transfer*, 218:124770, 2024.
- 790 [13] Eric Parish and Karthik Duraisamy. Non-markovian closure models for large eddy
 791 simulations using the mori-zwanzig formalism. *Phys. Rev. Fluids*, 2:014604, Jan 2017.
- 792 [14] Eric Parish and Karthik Duraisamy. A unified framework for multiscale modeling using
 793 the mori-zwanzig formalism and the variational multiscale method. *ArXiv*, 12 2017.

- 794 [15] Eric Parish and Karthik Duraisamy. *Coarse-Graining Turbulence Using the*
795 *Mori-Zwanzig Formalism*. Cambridge University Press, Cambridge, 2025.
- 796 [16] Carl Edward Rasmussen and Christopher K. I. Williams. *Gaussian Processes for Ma-*
797 *chine Learning*. The MIT Press, 2006.
- 798 [17] Adam Thelen, Xiaoge Zhang, Olga Fink, Yan Lu, Sayan Ghosh, Byeng D. Youn,
799 Michael D. Todd, Sankaran Mahadean, Chao Hu, and Zhen Hu. A comprehensive
800 review of digital twin – part 1: modeling and twinning enabling technologies. *Structural*
801 and *Multidisciplinary Optimization*, 65(12), 2022.
- 802 [18] Carlos A. Vargas Venegas, Daning Huang, Patrick Blonigan, and JohnTencer. Physics-
803 infused reduced-order modeling for analysis of multi-layered hypersonic thermal protec-
804 tion systems, 2025.
- 805 [19] Yongyong Xian, Baisong Pan, and Luping Luo. A new model updating strategy with
806 physics-based and data-driven models. *Structural and Multidisciplinary Optimization*,
807 64(1), 2021.
- 808 [20] Yin Yu, John Harlim, Daning Huang, and Yan Li. Learning coarse-grained dynamics
809 on graph. *arXiv preprint arXiv:2405.09324*, 2024.